

Design and Implementation of Full Field-Optical Coherence
Tomography on an Olympus IX73 Microscope

by

Rahul Thakur

A Thesis submitted to Faculty of Graduate Studies at
The University of Manitoba
in partial fulfillment for the degree of

MASTER OF SCIENCE

Department of Electrical & Computer Engineering
University of Manitoba
Winnipeg

Copyright© 2017 by Rahul Thakur

Abstract

Optical Coherence Tomography (OCT) has established itself as an important imaging technology for biomedical and industrial applications. In this thesis, we describe the design and implementation of a novel Full-Field OCT optical module that is specifically designed to fit inside an Olympus IX73 inverted microscope. We describe the design, components, and implementation of this novel optical module in detail. The resulting FF-OCT setup (microscope and OCT optical module) can be used as either a Time-Domain system or a Fourier-Domain (swept-source) system, without the need for considerable changes to the OCT optical module. However, we used our FF-OCT setup to implement a Time-Domain FF-OCT system. We describe our FF-OCT system's data acquisition process and Graphical User Interface (GUI) in detail, and we present imaging results obtained for samples comprised of stacks of glass coverslips.

Acknowledgements

The completion of my Master of Science would not have been possible without the guidance of my advisor, Dr. Sherif Sherif. I would like to express my deepest appreciation to him for supporting me in every stage of my research and for motivating me to move forward. I respect and thank Dr. Sherif for accepting me as his student, and for showing trust in me throughout this project. The experience and knowledge I have gained while working with him over the past few years have been extremely valuable.

Furthermore, I would also like to thank Dr. Arkady Major and Dr. Francis Lin for serving as committee members for my project. Dr. Major's suggestions were indispensable in helping me to set up the laser used in my research.

Moreover, I would especially like to thank from the bottom of my heart my friend and colleague, Dr. Fernando Saccon, for his support and guidance in the lab.

Finally, I would like to pay my respect and love to my family and Lord Krishna, who have both been a source of emotional support in every conceivable way. I would also like to sincerely extend my regards to my brother's family for supporting me and helping to make this happen in an easy and efficient way. The sacrifices made by my parents, however, are beyond words.

Table of Contents

Abstract.....	i
Acknowledgments.....	ii
List of Tables.....	vi
List of Figures.....	vii
Chapter 1 Introduction	
1.1 Motivation.....	1
1.2 Thesis Contributions.....	1
1.3 Thesis Structure.....	2
Chapter 2 Optical Coherence Tomography	
2.1 Optical Imaging Techniques.....	3
2.2 Introduction.....	4
2.3 Working Principle of OCT.....	5
2.4 Time Domain OCT (TD-OCT)	9
2.5 Spectral Domain OCT (SD-OCT)	12
2.6 Swept Source OCT.....	13
2.7 Full-Field OCT.....	16

Chapter 3 Design and Experimental Setup of our novel FF-OCT system

3.1 Introduction.....	19
3.2 Olympus IX73 Microscope and Overall Design of our FF-OCT System.....	19
3.3 FF-OCT Module and Hardware.....	21
3.3.1 Design Challenges and Solutions.....	21
3.3.2 Implementation of FF-OCT system.....	24
3.3.3 List of Components of our FF-OCT system.....	29

Chapter 4 Graphical User Interface of our novel FF-OCT system

4.1 Data Acquisition and Control Signals.....	31
4.2 Graphical User Interface (GUI).....	34
4.2.1 Front Panel.....	34
4.2.1.1 Camera Control switches.....	34
4.2.1.2 Laser Control switches.....	35
4.2.1.3 Piezo-electric Motor Control switches.....	36

Chapter 5 Experimental Results.....	39
-------------------------------------	----

Chapter 6 Conclusion and Future Work.....	47
---	----

Appendix 1 Phase Unwrapping in Fourier Domain based FF-OCT.....	48
---	----

Appendix 2 NKT Laser LabView Instructions and Register Values.....	51
--	----

Appendix 3 Matlab Code and Block Diagram of LabView Code.....	53
References.....	55

List of Tables

Table 1. Differences between SS-OCT and SD-OCT[22]	15
Table 2. List of all the components of the FF-OCT system.....	30
Table 3. Register Commands for our laser in LabView	51
Table 4. Telegram Message received from our Laser in Labview	52

List of Figures

Figure 1. Michelson Interferometer showing the sample and reference arm.	7
Figure 2. FD-OCT setup with a spectrometer consisting of a grating and CCD.....	13
Figure 3. Schematic Diagram of a Swept-Source OCT System.	14
Figure 4. FF-OCT Schematic Diagram	18
Figure 5. Architecture of our FF-OCT system.	20
Figure 6. Empty deck in the Olympus IX73 to configure FF-OCT on Breadboard.	21
Figure 7. Image of an Olympus IX73 Microscope.	22
Figure 8. First design with horizontal setup	24
Figure 9. Schematic of our FF-OCT setup.	26
Figure 10. 3D picture of the FF-OCT setup on a breadboard.....	26
Figure 11. Optical module of our FF-OCT system.....	27
Figure 12. Supercontinuum Laser EXR-15 and RF driver.	28
Figure 13. SuperK Select Acousto-optic Tunable Filter.	28
Figure 14. SuperK Connect Fiber delivery system.....	29
Figure 15. FF-OCT module in the second deck of our Olympus IX73 microscope.	32
Figure 16. Olympus IX73 Microscope with FF-OCT module and Camera underneath.	33
Figure 17. Front Panel of our FF-OCT GUI.....	37
Figure 18. Extended Control panel of Camera	38
Figure 19. Micro glass coverslip (Sample).....	39
Figure 20. B-scan showing the raw data from 3 coverslips.....	40
Figure 21. B-Scan showing resultant image of 3 coverslips.....	41
Figure 22. B-Scan showing raw data from 4 coverslips.	42

Figure 23. B-Scan showing resultant image of 4 coverslips.....43

Figure 24. B-Scan showing raw data from 6 coverslips.44

Figure 25. B-Scan showing resultant image of 6 coverslips.....45

Introduction

1.1 Motivation

Optical Coherence Tomography (OCT) is a non-invasive, non-contact, non-ionizing subsurface imaging technique that offers a high degree of resolution. Developed in 1991, OCT is a relatively new technique [1] that works on the basic principle of white light interferometry, with imaging being performed via the processing of interference images. Optical path difference matching is critical in interferometric process, and this requires precision in order to provide interference and good results. As will be discussed in Chapter 2, there are a number of different types of OCT, but Full-Field OCT, which is a parallel-imaging and fast acquisition method that takes 2D en-face images, has made significant contributions to the medical industry that range from the imaging of vascular plaque to cancer tissues. This project is motivated by the desire to develop an imaging system using the available infrastructure and resources, specifically the addition of an optical module to the Olympus IX73 microscope, which represents a novel innovation.

1.2 Thesis Contributions

1. The design and implementation of FF-OCT on an Olympus IX73 microscope.
2. The development of a graphical user interface to communicate and the synchronization of all of the components.
3. The processing of Time-Domain data using a simple demodulation technique based on Hilbert Transform.

1.3 Thesis Outline

Chapter 1 provides a brief introduction to this project and outlines the structure of the thesis.

Chapter 2 gives a basic introduction of OCT and provides an in-depth review of different OCT methods, such as Time-Domain OCT, Fourier-Domain OCT, and Swept-Source OCT. In addition, given this thesis' focus on FF-OCT, this chapter also provides an extensive discussion of this method.

Chapter 3 describes various aspects of the FF-OCT optical module, including its design, as well as challenges faced while designing and their solutions. Moreover, this chapter details the process of joining the FF-OCT optical module to an Olympus IX73 microscope and the components used to do so, including the high-power Class 4 laser. Details of all the parts are given in tabular form, which can be used as a “recipe” for the system.

Chapter 4 describes the system's Graphical User Interface (GUI) and the data acquisition protocols, which describe all function parameters and act as an instruction booklet. The GUI was made using LabView software and is very simple to use.

Chapter 5 presents our experimental results.

Chapter 6 presents our conclusions and suggestions for possible future work.

Optical Coherence Tomography

2.1 Optical Imaging Techniques

Although it has numerous industrial applications, optical imaging is widely used in the biomedical field for diagnosing various medical problems due to its advantages over other imaging techniques [2]. Indeed, current advanced imaging techniques, such as X-ray, CT scan, MRI, Ultrasound, and Photoacoustic Imaging, each have limitations. Conversely, Optical Coherence Tomography (OCT) offers a number of advantages due to being a cost-effective in-vivo, non-invasive, and non-ionizing technique that can produce real-time, high-resolution results. Other imaging techniques, such as X-ray and ultrasound, lack OCT's level of resolution. The main principle of optical-imaging techniques is to capture the backscattered light from either abnormal tissues, lesions, or any other foreign objects as well as from normal tissues in order to detect any abnormalities in the body. Since water is the main constituent of our bodies in general, and tissues in particular, light passing through it will absorb and scatter, which in turn assists in detecting abnormalities. In some techniques, like Fluorescence imaging [3], the patient is injected with a certain type of dye (DAPI) that attaches to A-T rich regions of their DNA. When the light is incident at a particular wavelength from a source, a different emerging wavelength is observed due to energy excitation and differences. Similarly, each technique functions differently based on its underlying principle and the equipment it uses. The topic of focus in this thesis is OCT, which involves imaging an object slice by slice. OCT uses light as the source and applies an interferometric technique to perform cross-sectional, or subsurface, imaging. This technique can provide real-time images more quickly and with better resolution images than the above-mentioned techniques. This chapter provides an overview of optical coherence

tomography in general, as well as a discussion of some of its variants, such as Time-Domain OCT and Fourier-Domain OCT, that outlines their working mechanisms, their advantages, and their limitations.

2.2 Introduction

Optical coherence tomography is an established, though relatively new, imaging modality. OCT was developed in 1991 [1] as a non-invasive imaging technique that would be able to produce images of 2D or 3D structures via cross-sectional tomographic imagery. OCT can either produce a series or an array of 2D images that can be accumulated together (processed) or 3D images, or both. Furthermore, it is more approachable due to its ability to produce high-resolution images, as well as other properties such as non-ionization. OCT fills the middle ground between confocal microscopy and ultrasound by simultaneously offering high resolution and imaging depth. Standard clinical ultrasound applications have an imaging depth of several cms, but the resolution quality pales in comparison to OCT at 150 micrometers to 1-10 micrometers, respectively[4][5]. OCT is frequently compared to ultrasound because these technologies work on the same principle of acquiring backscattered/reflected light. However, whereas ultrasound uses sound, OCT uses light as its radiation source. With ultrasound, a higher frequency will produce a higher resolution, but this is limited by the attenuation of the sound. Hence, this leads to reduced penetration depth, which thus forces a trade-off between resolution and imaging depth.

Resolution is a key feature that distinguishes OCT from other imaging technologies. Axial resolution is defined as a system's capability of distinguishing between two spots that are parallel to the direction of light; conversely, lateral resolution is a system's ability to distinguish between two different spots that are perpendicular to the direction of light. Whereas the former is solely

dependent on the light source's coherence properties, the latter is based on the system's optics [5]. This indicates that the selection of an appropriate light source and optics can play an important role depending on the needs of the optical system or the sample to be imaged.

During imaging, the level of resolution, penetration depth, and signal to noise ratio will depend on the sample's scattering and absorption properties. A tissue is comprised of about 70% water [6], with the remainder being made up of varying levels of oxy-hemoglobin and deoxy-hemoglobin, fats, and lipids depending on the type of sample chosen. We consider the two important factors: the absorption coefficient μ_a , and the scattering coefficient μ_s . Based on the different values of the absorption and scattering coefficients, we consider different attributes related to the scattering phase function[7] and how light will act when it enters and reflects back from the tissue. Our ability to comment on different qualities of the absorption or scattering of light, as well as Rayleigh and Mie scattering, is wavelength dependent. For example, in a thick tissue, which has greater absorption properties, we lose optical power and receive a weak output. Due to the turbid tissue, the resolution and imaging depth is affected, which in turn requires more power. Various researchers have reported results that indicate changes in the optical behavior or properties of a diseased retina (in the red blood vessels) that has been imaged using backscattered light via OCT [8]–[10].

2.3 Working Principle of OCT

In this section, we will discuss the basic principle of OCT; namely, the use of interferometric techniques and the collection of an array of cross-sectional images. OCT's working methodology is most easily understood by comparing it to a known technology, such as ultrasound. OCT and ultrasound are comparable because they both have a source and their detectors both collect the echo and the backscattered light coming from the sample, respectively. However, unlike

ultrasound, OCT works with a light source that can range from broadband to near infrared or swept-source laser, depending on the system's needs. The use of different types of sources can result in the different hardware configurations that produce the different forms of OCT, such as Time-Domain OCT (TD-OCT), Spectral-Domain (SD/FD-OCT) and Swept-Source OCT (SS-OCT). The basic design implementation uses a Michelson interferometer, which has two arms with a beam splitter in the middle (Figure 1). One arm is referred to as the sample arm and the other is referred to as the reference arm. The light is illuminated from one end, and the beam splitter divides it into two equal halves, sending one part to the sample and the other part to the reference arm. After traveling through the sample/surface, the light is reflected back to the beam splitter where the reflected light from the reference mirror is combined and interference is shown on the detector. In this design, we use Low-Coherence Interferometry [11] as well as a delay scanning mechanism, which is performed by the mirror at the reference arm and which produces a known delay that can be easily calculated if needed. Matching the optical path difference between the two arms is one of the key factors for working with OCT; furthermore, constructive interference is observed at intensity maximum.

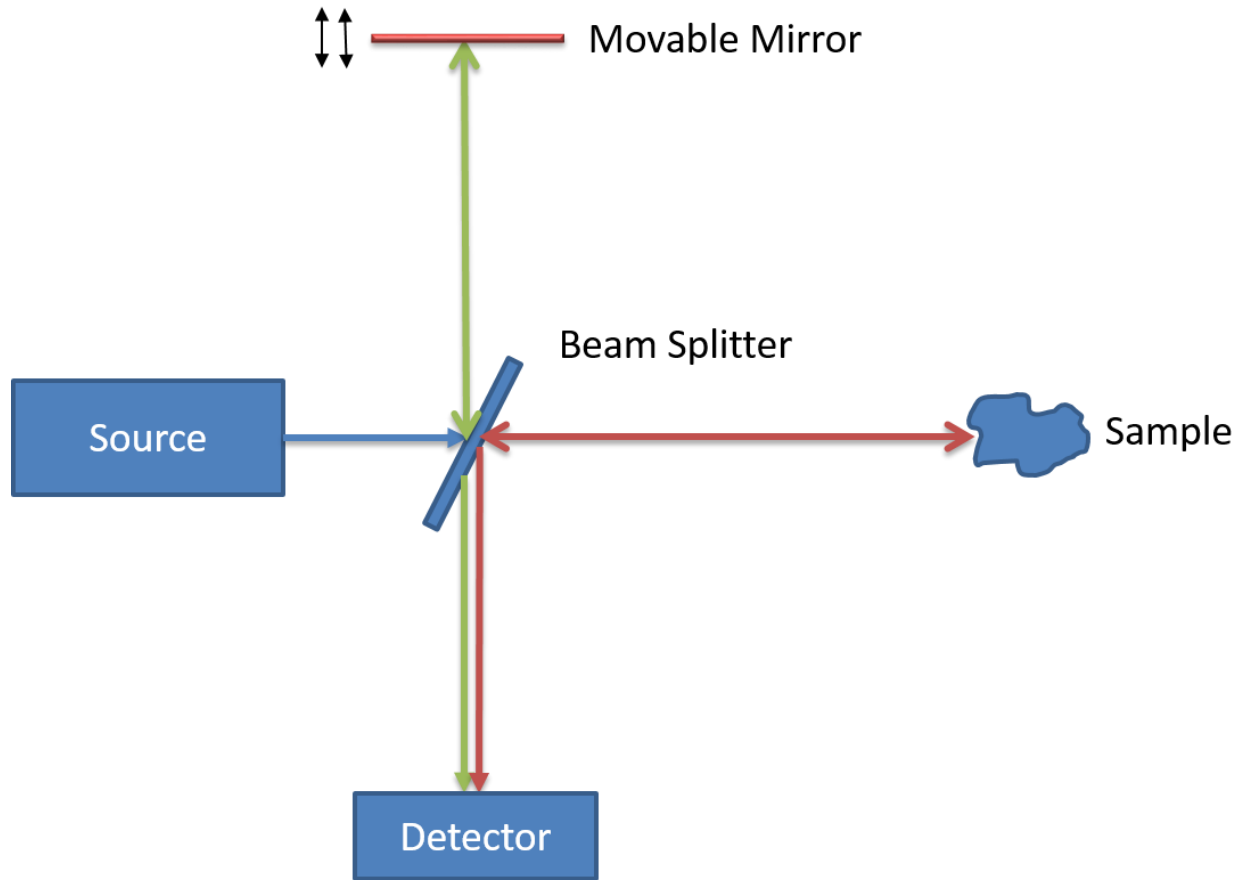


Figure 1. Michelson Interferometer showing the sample and reference arm.

Optical imaging uses a dual-scanning process, referred to as A-scans and B-scans, and the combination of the two produces a 2D image that can be used to get results from and to perform signal processing. The A-scan is known as the depth scan of the sample, while the B-scan is referred to as an array of A-scans in the transverse direction. The produced interference signal can be considered as the field autocorrelation of the light source that provides the information about the axial resolution. The axial resolution Δz is inversely proportional to the bandwidth of the light source $\Delta\lambda$

$$\Delta z = \left(\frac{2 \ln 2}{\pi}\right) \left(\frac{\lambda^2}{\Delta \lambda}\right) \quad (1)$$

where λ is the center wavelength of the light source, and Δz and $\Delta \lambda$ are the FWHM of the autocorrelation and the power spectrum, respectively[11].

The different categories of OCT—namely, TD-OCT, SD-OCT, SS-OCT and FF-OCT—are differentiated based on the system design and the light source. TD-OCT uses a similar technique as the one discussed above for LCI, with two arms, a beam splitter, and a broadband source. However, since TD-OCT provides A and B-scans by scanning the mirror in a delayed line over the whole sample, it has a slow acquisition speed.

Conversely, in Spectral-Domain OCT, the reference arm is kept fixed and a spectrometer is used at the detector end because it is more dependent on the frequencies reflected back from different depths. This variant of OCT, also known as Fourier-Domain OCT, has a faster acquisition speed than TD-OCT because it eliminates the need to mechanically move the mirror. In the SS-OCT approach, the source is replaced by a fast tunable laser that sweeps the desired wavelength, and a camera, rather than a spectrometer, is used for detection. FF-OCT is different from these other variants such that it does not use A-scans or B-scans; rather, it takes a full en face image of the sample. Furthermore, it does not require continuous scanning through the mirror and it grabs all of the A-scans in one shot, thereby eliminating the speed constraints. However, to capture different positions, the mirror must be moved for a few steps, which are known as the phase unwrapping technique. In addition, this technique requires a CCD camera, but it is still much faster and has shown to improve lateral resolution [12]. All of these approaches are discussed in detail in upcoming sections.

2.4 Time-Domain OCT (TD-OCT)

Time-Domain OCT is the first type of OCT [1] technique to use Low-Coherence Interferometry. A simple TD-OCT design consists of a Michelson Interferometer with a mirror that can be moved to produce a variable delay. Mathematically, this can be represented for both monochromatic and low-coherence sources. The equations given below are initially for monochromatic waves and lead to the low-coherence source, which is of interest to us:

A complex plane wave is expressed as:

$$E_{so} = E_0 e^{-ik(\omega)z}, \quad (2)$$

where $k=2\pi/\lambda$.

The reference and sample arm light beam are shown by equations (3) & (4):

$$E_r = -(1/\sqrt{2}) E_{so} \quad (3)$$

$$E_s = i(1/\sqrt{2}) E_{so} \quad (4)$$

After the backscattering from the sample and the reference arm, the equations become:

$$E_{r2} = r_r \left(\frac{1}{\sqrt{2}} \right) E_{so} e^{-i2kl_r} \quad (5)$$

$$E_{s2} = -r_s \left(\frac{i}{\sqrt{2}} \right) E_{so} e^{-i2kl_s} \quad (6)$$

Due to reflection off of the mirror, the phases of the above-mentioned equations change by 180, which also changes the sign. After recombining through the beam splitter, E_D becomes[13]:

$$E_D = E_R e^{-i2kl_r} + E_S e^{-i2kl_s} \quad (7)$$

Squaring E_D , which is the irradiance factor on the detector arm as the electric field is not detected, results in the loss of the phase information and allows the complex degree of coherence to be obtained as:

$$I_D = |E_D|^2 = I_R + I_S + \text{Re}\gamma(Z)_{11} \sqrt{I_r} \sqrt{I_s} [e_r^{+i2k(l-l)_S} + e_r^{+i2k(l-l)_S}] \quad (8)$$

This equation can be simplified as,

$$I_D = I_R + I_S + 2\text{Re}\gamma(Z)_{11} \sqrt{I_r} \sqrt{I_s} \cos(2k\Delta l) \quad (9)$$

Since $k=2\pi/\lambda$ is known, the Doppler shift in the TD-OCT resulting from the movable reference arm can be added, thereby giving the constructive and destructive interference in the detector arm.

$$I_D = I_R + I_S + 2\text{Re}\gamma(Z)_{11} \sqrt{I_r} \sqrt{I_s} \cos(2kf_D l) \quad (10)$$

where $f_D = 2v_M/\lambda$, is the Doppler shift.

The above analysis is for a single frequency or a monochromatic light and can be extended for a low-coherence light that has a finite bandwidth. For the following equations, we have a broadband source, a 50/50 beam splitter, and two arms. The reference and the sample are denoted by E_r and E_s , respectively. A detector arm containing components of both arms is expressed as in Equations (11) & (12):

$$E_R(\omega) = E_r(\omega) \exp[-jk_r(\omega)l_r] \quad (11)$$

$$E_s(\omega) = E_r(\omega)\exp[-jk_s(\omega)l_s] \quad (12)$$

where l_r and l_s are the distance of reference and the sample, respectively, and E_r and E_s are the reflection amplitude, and k_r and k_s are the propagation constants. The sum of these waves as interference picked up by the detector is given by (13):

$$i_D \propto \text{real} \left\{ \int_{-\infty}^{\infty} s(\omega) \exp[-j\Delta\phi(\omega)] \frac{d\omega}{2\pi} \right\} \quad (13)$$

$$\Delta\phi(\omega) = k_s(\omega)l_s - k_r(\omega)l_r \quad (14)$$

Equation (14) represents the phase mismatch. A non-dispersive media with the same propagation constant mentioned in (14) can be extended using the 1st order Taylor expansion, thereby producing Equation (15):

$$\Delta\phi(\omega) = k(\omega_0)(\Delta l) + k'(\omega_0)(\omega - \omega_0) \quad (15)$$

By substituting, the interferometric signal and the values of phase delay and group delay can be obtained as:

$$I_d(\Delta l) \propto \text{real} \left\{ \exp[-j\omega_0\Delta\tau_p] \int_{-\infty}^{\infty} S(\omega - \omega_0) \exp[-j(\omega - \omega_0)\Delta\tau_g] d(\omega - \omega_0) / 2\pi \right\} \quad (16)$$

$$\Delta\tau_p = k(\omega_0)/\omega_0(2\Delta l) = (2\Delta l)/v_p \quad (17)$$

$$\Delta\tau_g = k'(\omega_0)(2\Delta l) = (2\Delta l)/v_g$$

Here, I_d is the Fourier transform of the power spectral density, and it represents the autocorrelation function referring to Wiener-Khinchin theorem[13] [14][15].

TD-OCT has emerged as a highly productive and successful technology that has been used for a variety of applications in fields ranging from medicine to industry. For example, it has been proven to be a successful tool in stent assessment[16], retinal imaging, and it has been used extensively in ophthalmology. Some recent studies have focused on its application for optical identification of documentation [17], glaucoma detection [18], and blood flow imaging in murine brains [19].

2.5 Spectral-Domain OCT (SD-OCT)

Spectral-Domain OCT is another type of OCT that works on the same principle of interferometry. However, unlike Time-Domain OCT, it does not have a movable reference arm for scanning and producing a delay; rather, both arms are fixed and there is a spectrometer at the detector end that detects the wavelength dependent backscattered light. As a function of the spectrometer which consists of a grating and a CCD detector. The grating separates the different wavelengths coming towards the detector. SD-OCT's fixed reference arm gives it a number of advantages over TD-OCT, such as improved sensitivity, higher acquisition speed, and deeper penetration depth. Interestingly, SD-OCT is as old as TD-OCT and it was proposed in 1995 [20] for these very advantages. However, these benefits were not realized in practice until 2002, when Maciej et al.[21] showed that retinal imaging via FD-OCT produced superior results. SD-OCT is more sensitive than TD-OCT by a factor of $N/2$ [22]. Figure 2 below depicts the setup of the SD-OCT.

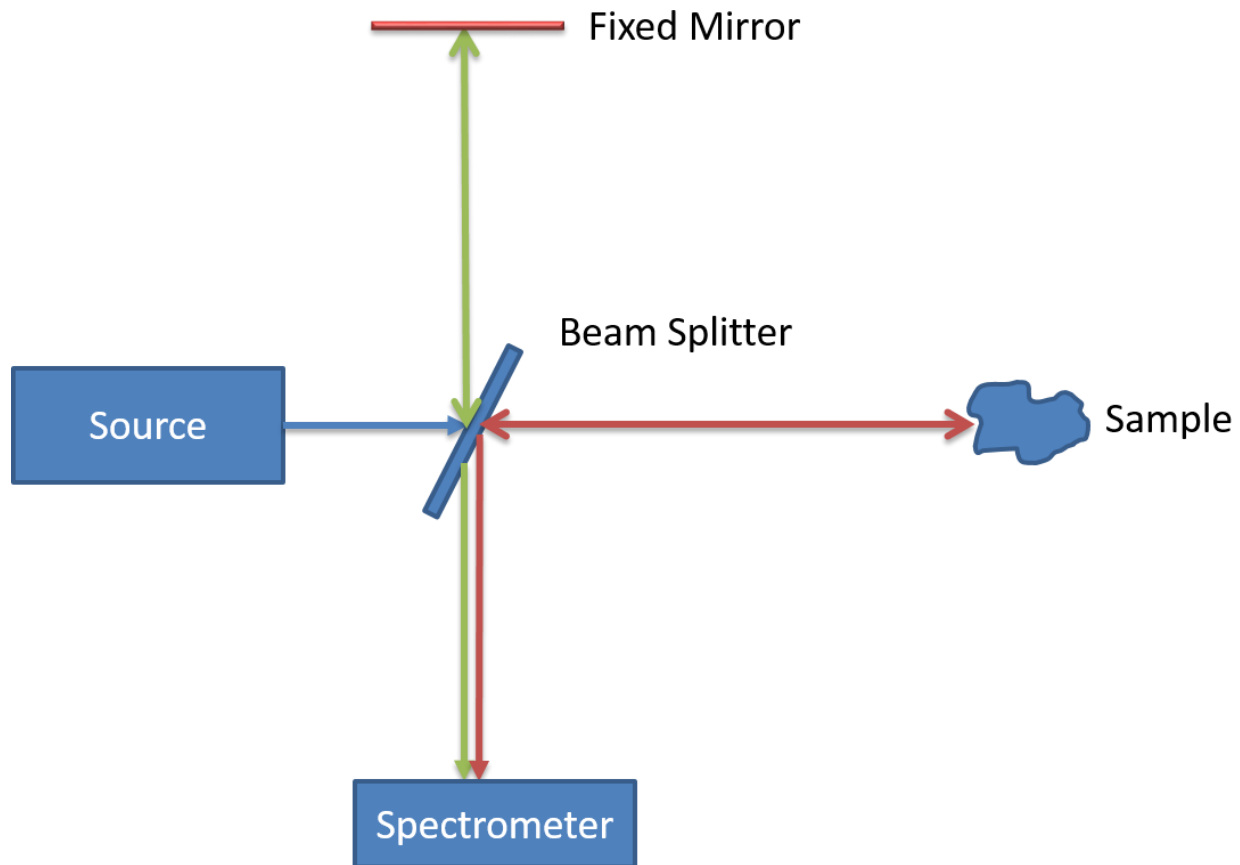


Figure 2. FD-OCT setup with a spectrometer consisting of a grating and CCD.

2.6 Swept-Source OCT

Swept-Source OCT, which is another type of FD-OCT, uses a fast tunable laser as a source. The laser sweeps off in a narrowband frequency and has equally spaced wavenumbers that are backscattered through the reference and the sample. The SS-OCT system acquires the interferometric signal after the beam splitter combines the two signals from reference and sample arm which is detected by the CCD camera alone, thus removing the need for an external grating.

Figure 3 shows the schematic diagram of the SS-OCT setup.

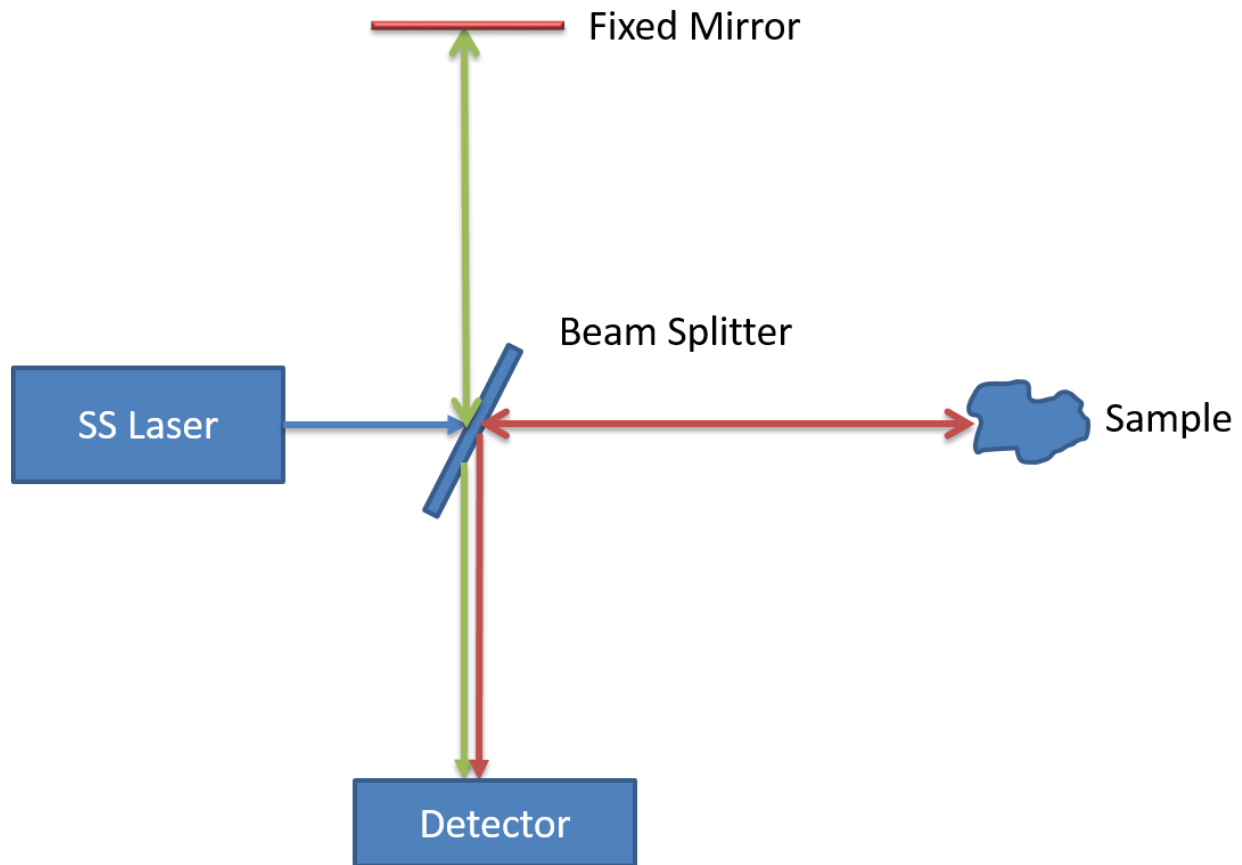


Figure 3. Schematic Diagram of a Swept-Source OCT System.

Practically speaking, this system does not have any moving parts, and it is considered to be an efficient and faster system for higher acquisition speeds. Table 1 shows the differences between, and relative advantages of, the SS-OCT and SD-OCT systems [22].

Properties	Swept Source OCT	SD-OCT
Heterodyne Detection	Yes	No
Speed	Comparable	Comparable
Light Source	Complex	Simple
OCT System	Simple	Complex

Spectral Band	1300 nm	800 nm
SNR drop-off	No	Yes
Balanced Detection	Yes	No

Table 1. Differences between SS-OCT and SD-OCT[22]

SS-OCT's features allow it to reduce noise and therefore prevent SNR drop-off. Moreover, it features heterodyne detection, which allows the negative and positive displacement of the interferometric signal shift from zero points to be detected. SS-OCT's high-speed and high-resolution capabilities are attributable to its ability to rapidly tune and sweep. These higher tuning and sweeping speeds allow for higher resolution, as depth resolution increases in proportion to the optical sweep range. As far as the intensity at the detector is concerned, the equations given below show a state wherein a wave from the reference and sample arm interferes and is detected as an interferometric signal.

Assuming the wave fields are plane waves and plane wave at a given incident is:

$$E^i(r, k^i) = A^i \exp[-jk^i \cdot r] \quad (18)$$

where the amplitude of vector $k^i = 2\pi/\lambda$ is known as a wave number and A^i is a constant representing the amplitude of the wave.

The reference and sample arm waves are then represented by Equations (19) and (20):

$$E_r(Z_r, k) = A^i \exp(-jkz_r) \quad (19)$$

$$E_s(Z_s, k) = \frac{A^i W}{4\pi Z_s} \exp(-jk(z_s)) * FT\{P(Z_s)\} \quad (20)$$

Here, Z_r and Z_s represent the signal from reference and sample, respectively, and assuming $Z_s = Z_r + \Delta z$ where Δz represents the path length difference [14].

The intensity at the detector can be expressed as:

$$I_D(k) \propto \left(2|A^i|^2 \frac{W}{4\pi Z_s} \right) \text{Re} \{ \exp(-jk\Delta z) * FT \{P(z)\} \} \quad (21)$$

Due to SS-OCT's tuning feature, the system is able to acquire evenly spaced wavenumbers N .

This process can be written as:

$$N * \delta k = \Delta k \quad (22)$$

where, $\delta k = \Delta k / \Delta t$ in which Δk = total bandwidth swept and Δt = sweep time. Using Equations (21) and (22), the depth scan range of SS-OCT can be written as:

$$D = \frac{N\pi}{2\Delta k} = \frac{\pi}{2\delta k} \quad (23)$$

Because of these equally spaced N wavenumbers, the inverse Fourier transform must be performed in order to obtain the data and to process the results. Consequently, the equation of the intensity at the detector changes as follows:

$$FT^{-1}\{I_D(k)\} = I_D(z) = 2|A^i|^2 \frac{W}{4\pi Z_s} P(Z_s) \quad (24)$$

2.7 Full-Field OCT

Full-Field OCT is different from the above-mentioned methods in that it takes en-face tomographic images that are orthogonal to the imaging axis. Instead of doing in-depth scanning

axially, FF-OCT takes several en-face images at different wavelengths penetrating at different depths and then performs the Fast Fourier Transform to extract the results. FF-OCT is a parallel imaging technique that uses a Linnik configuration; this configuration is similar to the Michelson interferometer, only it uses microscope objective lens in both arms for better resolution. There have been many advances in FF-OCT, with both ultra-high spatial resolutions of $\sim 1 \mu\text{m}$ and high speeds of 1.5 million A-lines/s having been achieved [12], [23]–[25][26][27][28]. FF-OCT's ability to produce higher transverse resolution is due to its use of identical microscope objectives. However, FF-OCT also requires a high degree of precision of alignment because of the optics involved and up to a degree of half a micrometer in order to meet the optimal optical path length. The numerical aperture (NA) of the objective lenses in the Linnik configuration plays an important role in the resolution of the image. While a lower NA lens strongly limits the transverse resolution, a high NA lens can increase the transverse resolution 10-20 times of that offered by the TD- and FD-OCT methods. Although the axial resolution is generally determined by the source's coherence length, in FF-OCT it is also affected by the lens' NA [29]. Furthermore, while FF-OCT can be used in several applications, it is primarily used in ophthalmology as tissues containing a high volume of water can sometimes affect the axial resolution due to the dispersion mismatch in the arms. As such, water-immersed objectives are used for correcting and increasing the resolution. For an increased imaging depth, especially for weakly scattering tissues, a high degree of detection sensitivity is required. This degree of detection sensitivity is dependent on the detector's full-well capacity. Unlike TD-OCT, where the sensitivity of the system can be estimated using the bandwidth of the light source, the sensitivity of the FF-OCT system can be estimated via the pixel capacity of capturing the photons and its sensitivity.

Figure 4 represents a schematic of a FF-OCT with a light source, objective lenses, a beam splitter, a reference mirror, and a CCD detector. The detectors used in this FF-OCT are area cameras that provides 2D en-face images containing an array of pixels. The captured information is then used for processing.

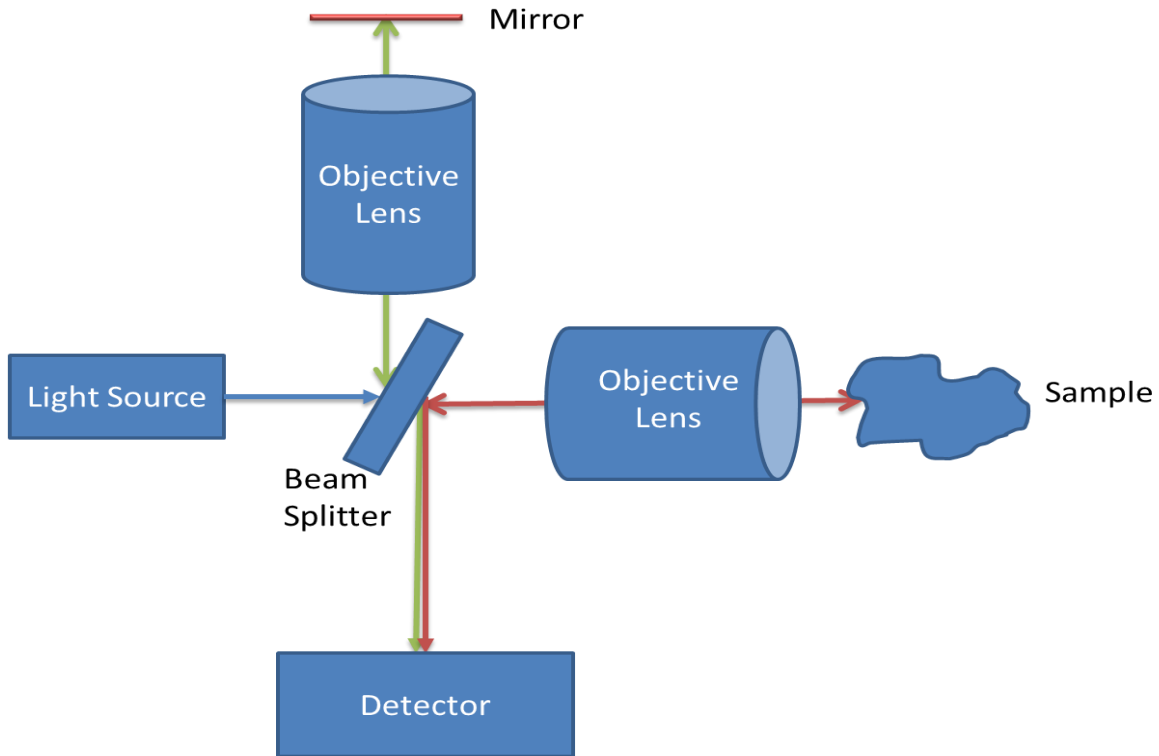


Figure 4. FF-OCT Schematic Diagram.

In our Time-Domain based FF-OCT, the acquisition is performed by standard technique of producing delay by reference arm and processing the raw data, however, in Fourier Domain based FF-OCT; the method of acquisition and performing signal processing on the raw data is based on Phase unwrapping technique mentioned in detail in Appendix 1.

Design and Experimental Setup of our novel FF-OCT system

3.1 Introduction

Chapter 1 and Chapter 2 provided a detailed overview of OCT and its different types, including Full-Field OCT, which is our topic of interest. This chapter will discuss FF-OCT's underlying principles and its constituent components, which will also be presented in a table in order to provide future researchers with a “recipe” for implementing a complete FF-OCT system. In addition, this chapter will also provide a brief introduction to the Olympus microscope, which is the feature that makes our system unique. Section 3.2 describes the microscope and the overall design of our FF-OCT system, which is set up in a small compartment. Section 3.3 describes the optical module and other associated parts. Section 3.3.1 discusses the challenges that arose in the design of our FF-OCT system and the solutions that were used to overcome them. Section 3.3.2 details the implementation of the FF-OCT module, and, finally, Section 3.3.3 provides a detailed list of the FF-OCT system's constituent components.

3.2 Olympus IX73 Microscope and Overall Design of our FF-OCT System

The driving idea behind this project was to develop a unique system that would use the available resources in an efficient manner. To this end, we chose to use an Olympus IX73 Microscope as the base for our Full-Field OCT system as they are capable of being used simultaneously. The Olympus IX73 is an inverted microscope that has outstanding live cell imaging capabilities in addition to being very flexible to different research needs. While its UIS2 infinity corrected optics microscope objectives make it highly useful for high-resolution fluorescence imaging, the

Olympus IX73 microscope can perform other routine imaging as well. There are two versions of the Olympus IX73: a one-deck system and a two-deck system. We elected to use the two-deck system because it features different compartments with different modules that can be easily removed in order to extend its research capabilities. Furthermore, it also has a simple cassette-like eject structure that can be replaced; specifically, it has two empty slots, removable and replaceable filters, and a removable high-power halogen lamp. In our FF-OCT setup, the second (upper) empty deck was placed exactly in alignment with microscope’s optics; specifically, the aperture provided for the camera beneath and the microscopes objectives at the top. Figure 5 illustrates the overall architecture of our FF-OCT system, showing the laser’s communication with the computer, the path light takes to the optical module and the flowing of data to the computer by the camera via USB. A detailed explanation of Figure 5 will be presented in the upcoming sections.

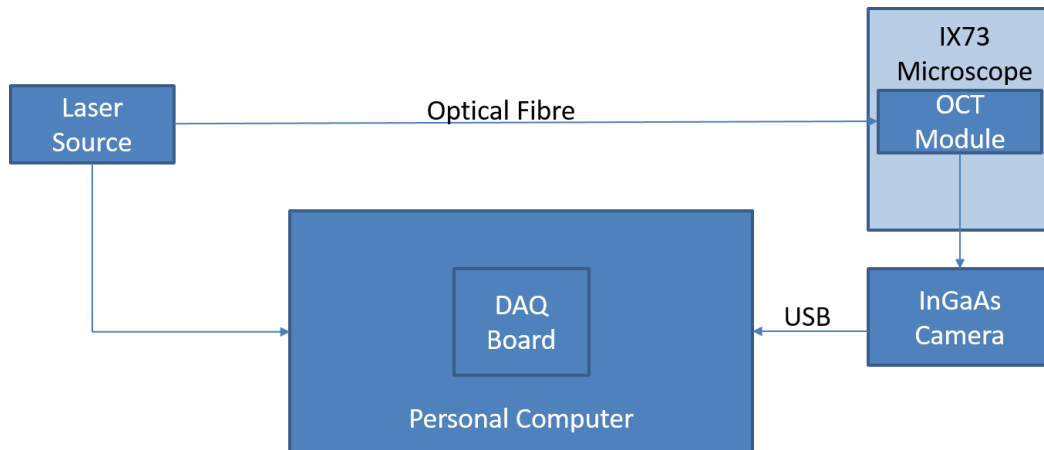


Figure 5. Architecture of our FF-OCT system.

3.3 FF-OCT Module and Hardware

This section discusses our FF-OCT’s design, implementation, and constituent components.

3.3.1 Design Challenges & Solutions

With a basic understanding of the two deck system of the microscope, we initiated the development of our optical module. We implemented our optical module on a breadboard taken from the upper deck. Out of the two images shown below, Figure 6 shows the empty slot where the FF-OCT is set up, and Figure 7 shows the Olympus IX73 microscope.

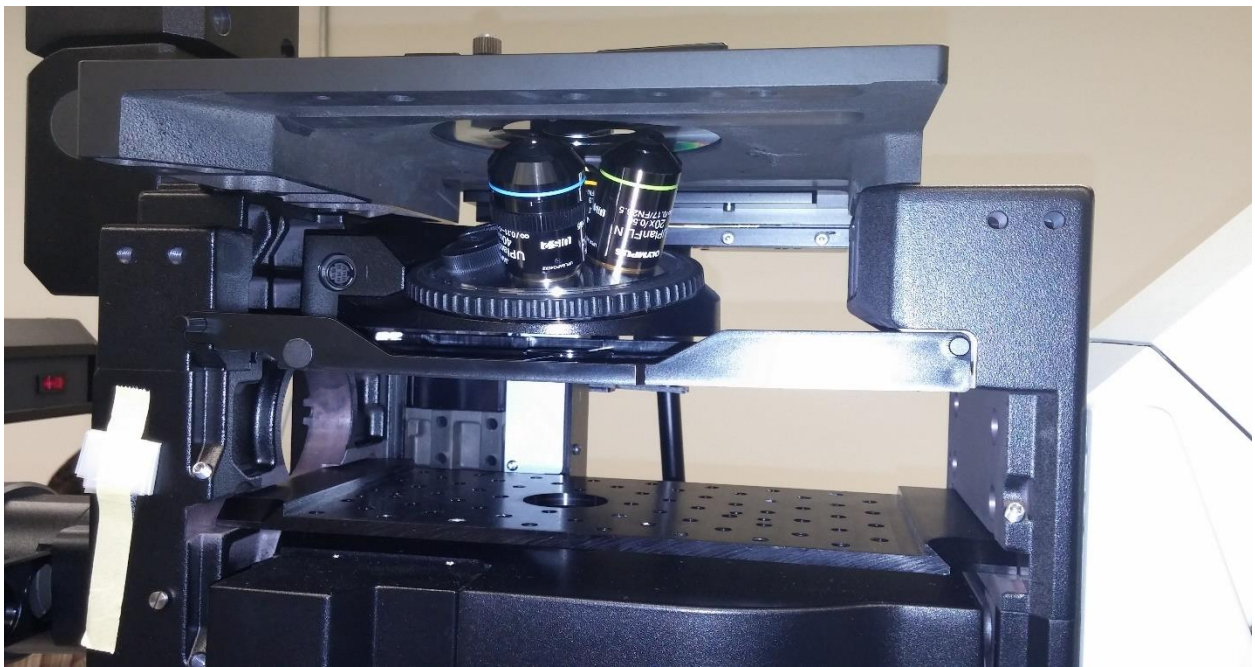


Figure 6. Empty deck in the Olympus IX73 to configure FF-OCT on Breadboard.



Figure 7. Image of an Olympus IX73 Microscope.

Of the numerous challenges we faced, the most important was the design of the optical module and how to implement the interferometric technique. We opted to use a Linnik interferometric configuration, which is the same as a Michelson Interferometer (i.e. it contains a beam splitter, a sample arm, and a reference arm) apart from the fact that it also has microscopic objectives in both arms, which provides it with high transverse resolution that is comparable to optical microscopy. However, the level of precision required during alignment is very high [35]. With all of these constraints in mind, two designs were shortlisted. The first design, shown in Figure 8, simply places all of the optics on a horizontal plane in line with the microscope. Since the length of the upper deck is about ~ 24 cm, there is ample space to create a Linnik configuration. However, after placing the beam splitter in line with the microscope camera's optics and aperture, we were left with ~ 15 cm in length; since the FF-OCT module required about ~ 14 cm,

we lacked the space to allow the piezoelectric motor/ reference mirror to move back and forth freely. The second design addressed this issue by featuring a 45° degree tilt that moved the piezoelectric motor out of line from the microscope. This can be seen coming out of the slot resting on the same breadboard but it has the advantage of providing a degree of freedom to move to its full range of 27mm. Figure 10 depicts the final FF-OCT design, as per the requirements. Its virtual replica was made in Solidworks along with the other parts required to mount the piezo and the mirror on top of it. Our design includes a beam collimator, a beam splitter, two microscope objectives (one in each arm), a reference and a sample arm. Another challenge was to overcome the losses while keeping the optical module sturdily aligned in a straight line. In response to this challenge, we used a cage system for the module because it is much more robust and it ensures that the optics are on an aligned plane. However, this required a very precise level of alignment due to the free space optics included. Another challenge faced was how to fill the objective lens' back aperture in order to avoid beam clipping and to reduce power losses. We compensated for this by using a reflective collimator with an output beam width of 8.5mm; this perfectly filled the objective's back aperture of 9mm. Hence, all the problems were solved with most appropriate solutions.

The details of our FF-OCT system's design, along with the list of parts and their specifications, are given in next section.

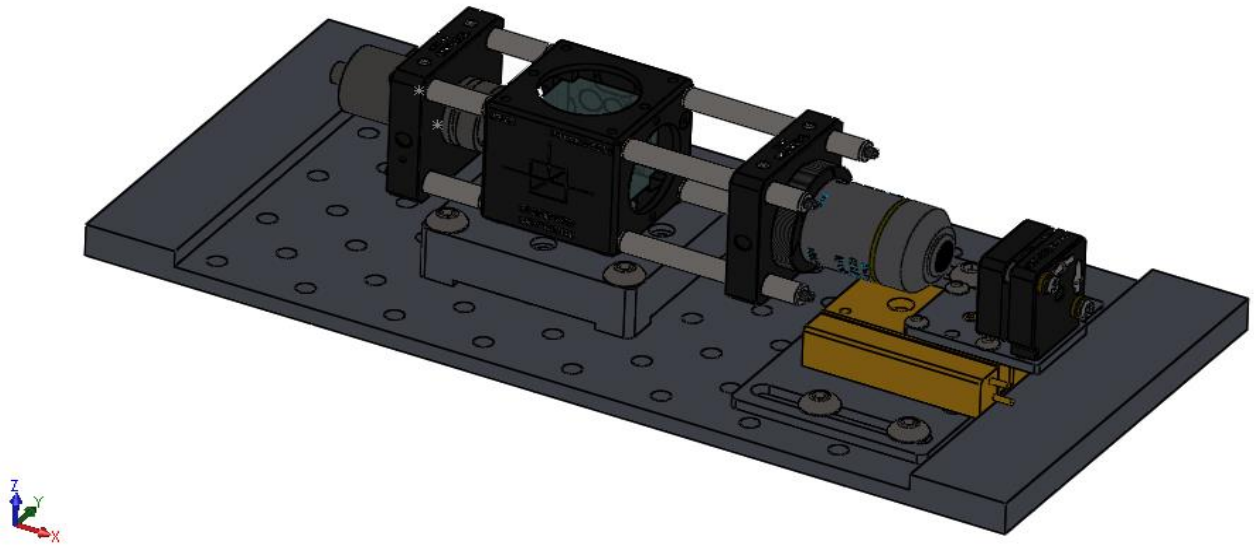


Figure 8. First design with horizontal setup.

3.3.2 Implementation of FF-OCT System

As mentioned in Section 3.3.1, our system used the Linnik Configuration. Figure 9 and Figure 10 show the schematic of the FF-OCT module and the 3D picture of the finalized design with the cage system, respectively. As shown in Figure 12, our light source was a Supercontinuum laser from NKT Photonics EXR-15 that featured: a broad bandwidth of 400-2400 nm with a repetition rate of 78MHz; two Acousto-optics tunable filters ranging from 1100-2000 nm with a filter bandwidth of ~ 6 nm (at 1310); and an output power of ~ 3.5 mW @1310nm. Our selected laser was a high-power, Class 4 laser that emitted its beam from a fixed aperture feeding into the Tunable filter (SuperK Select) (shown in Figure 13). The external RF driver, which sits under the laser, drives the AOTF and can be modulated to emit up to 8 different wavelengths simultaneously. The driver is connected to SuperK Connect, which is a Fiber Delivery System (FDS) (shown in Figure 14) that has two mirrors inside. This connection must be perfectly

aligned with the laser beam from the AOTF to achieve a coupling efficiency of ~30% (@1310nm). The light travels through the optical fiber to a silver reflective collimator producing an output beam of 8.5mm, which was explained in Section 3.3.1. After the collimator, we used a 50:50 beam splitter that had a working range of 1100-1600 nm and that was fixed in the middle of the cage system in order to divide the power equally between the sample and reference arms. The microscope objective had magnification of 10X in both the sample and reference arms for added transverse resolution. The field of view of our system at the sample is 2.2 mm which is calculated by using equation (25) below:

$$\text{Field of View} = \frac{\text{Eyepiece F.N.}}{M(\text{ob})} (\text{mm}) \quad (25)$$

Where, F.N. is 22, field number (field stop aperture) of the objective lens and M is the magnification of the objective lens. A highly reflective gold mirror with a reflectance of over 96% was mounted on top of the Newport piezoelectric motor, which featured an inbuilt linear encoder for high-precision movements and could travel up to 27 mm in incremental steps of 1 μ m. Finally, for detection, we used an InGaAs camera, Widy-640, from NIT, France that had a resolution of 640 x 512 pixels and a pixel pitch of 15 μ m. In brief, the light coming from the source is emitted through the collimator with a beam width of 8.5mm on the beam splitter; it is then divided in 50:50 ratios and passes through objectives by filling the objective's entire back focal plane with light; this light is then reflected back from the sample and reference arms, and the interference pattern is recorded by the camera. However, the novelty of this system is that it can also be referred as a Hybrid System. By switching the light source, this system can become a Time-Domain/SS-OCT, and all the other optics and software can work as a Full-Field OCT system working in the time and frequency domains for acquisition. Figure 11 depicts the actual FF-OCT module setup.

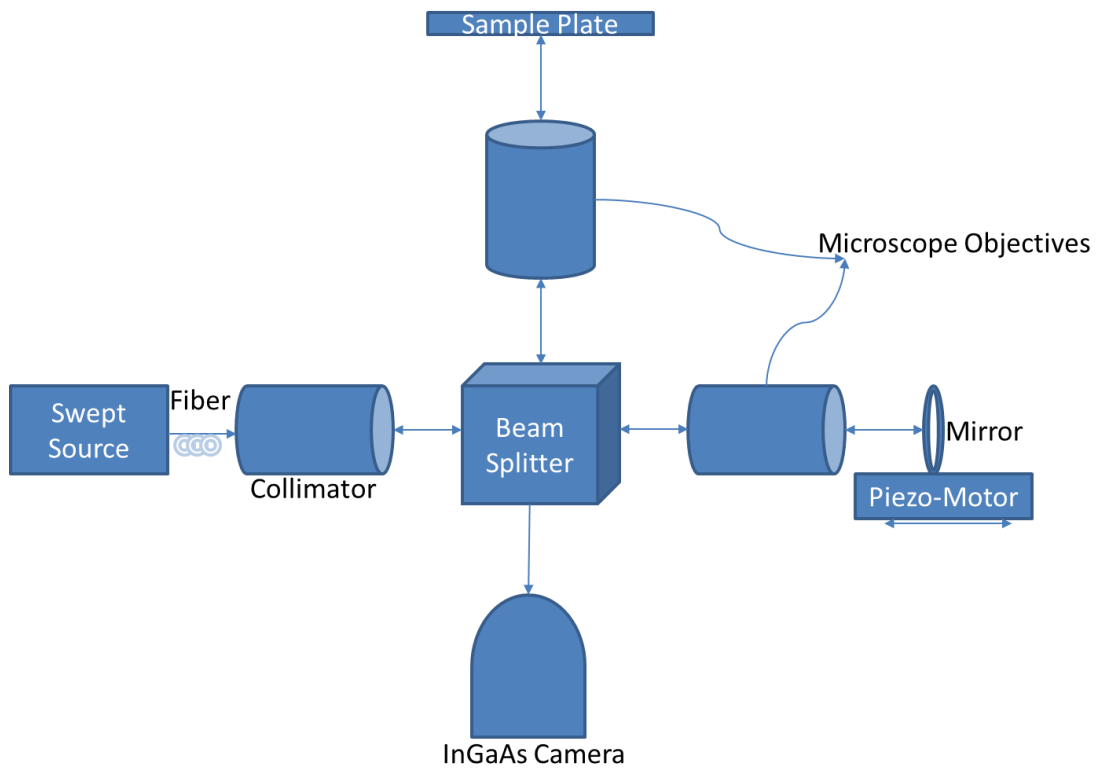


Figure 9. Schematic of our FF-OCT setup.

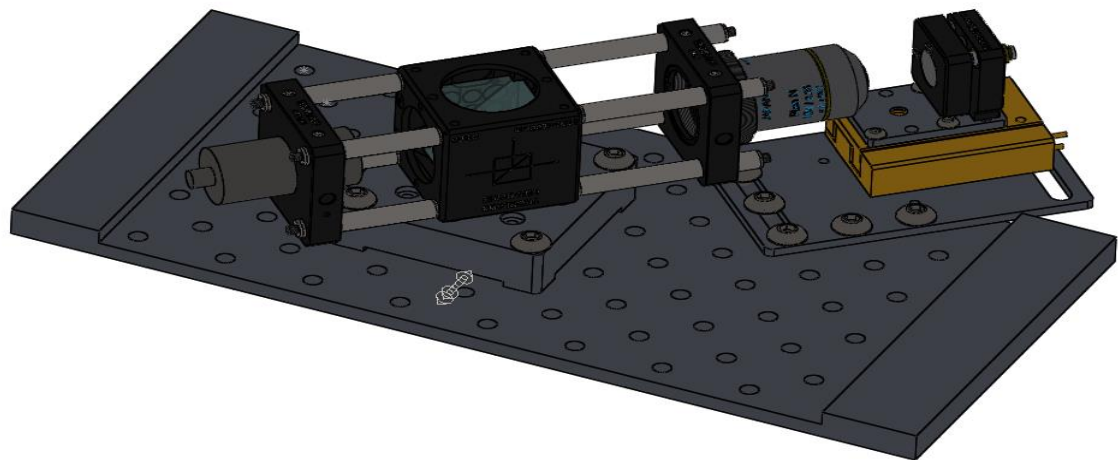


Figure 10. 3D picture of the FF-OCT setup on a breadboard.

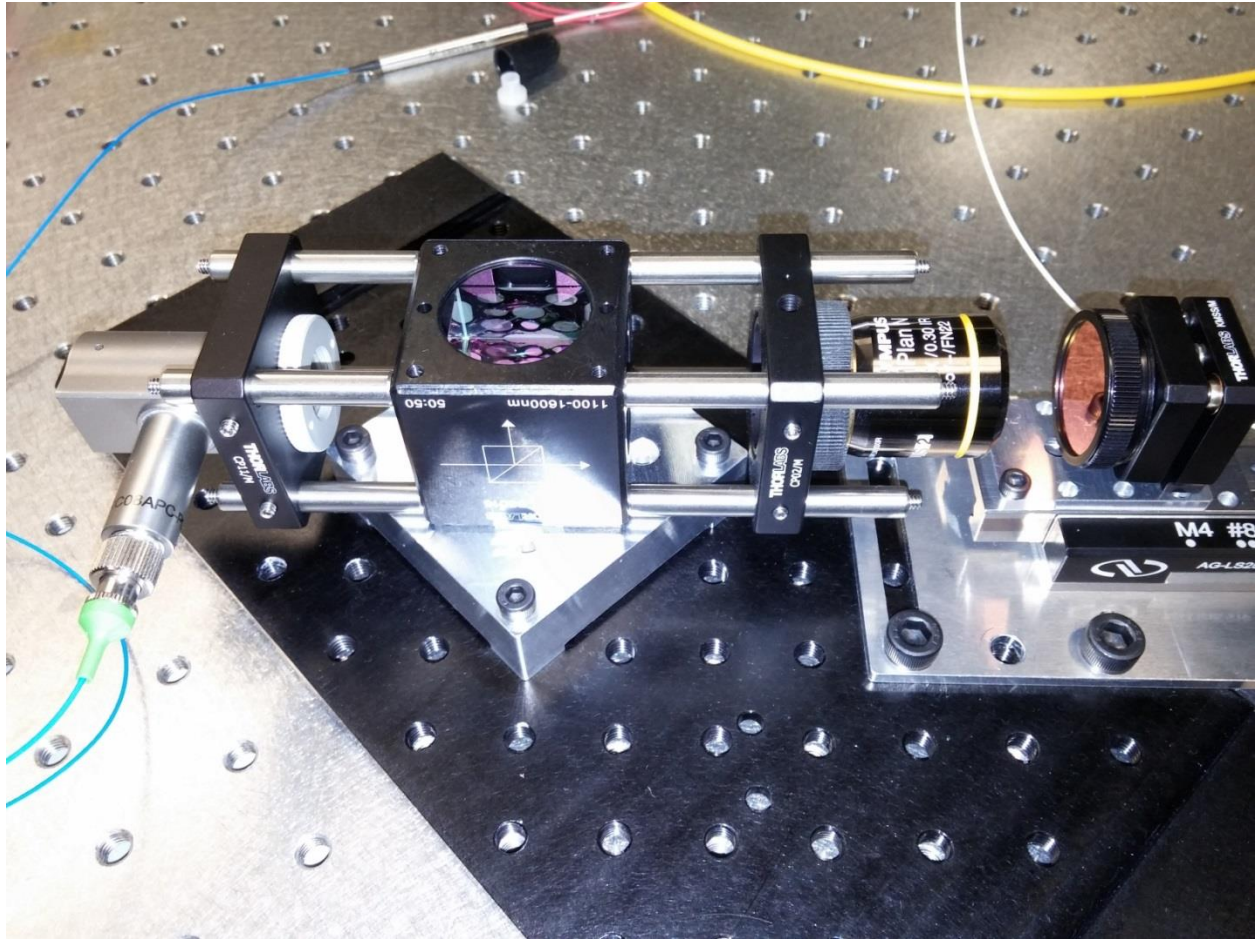


Figure 11. Optical module of our FF-OCT system.



Figure 12. Supercontinuum Laser EXR-15 and RF driver.



Figure 13. SuperK Select Acousto-optic Tunable Filter.



Figure 14. SuperK Connect Fiber delivery system.

3.3.3 List of Components of our FF-OCT system

The following table provides a full list of the components used in the system setup.

Component	Manufacturer	Model Number	Specification & Comments
Supercontinuum Tunable Laser	NKT Photonics	EXR-15	Tunable light source. Bandwidth 400-2000 nm.
RF Driver	NKT Photonics	A901-100	An external RF driver, controlling the AOTF filter.
SuperK Select	NKT Photonics	A203-245	AOTF Filter
SuperK Connect	NKT Photonics	A401-500	Fiber delivery system
Optical Fibre	NKT Photonics	FD6 Non-PM	FC/APC connector

Reflective Collimator	Thorlabs	RC08APC-P01	Beam width 8.5mm
Beam Splitter	Thorlabs	CM1-BS015	50:50 splitter
Microscope Objectives	Olympus	LMPLan N	10X Magnification, FN 22
Gold Mirror	Thorlabs	PF 10-03-M01	>96% reflectance
Piezoelectric Motor	Newport	Conex AGLS25-27P	Travel Distance 27mm.
InGaAs Camera	New Imaging Technologies	Widy-640V	640x512 pixels
Microscope	Olympus	IX73	Inverted Microscope
Breadboard	Olympus	N/A	Fits M6 screws and FF setup
Adapter Cage Plate	Thorlabs	CP11/M	Holds Collimator into Cage system
Cage Assembly Rod	Thorlabs	ER1.5-P4	Holds CP11/M and BS015
Cage Assembly Rod	Thorlabs	ER2-P4	Holds CP02/M and Objective
Adapter Cage Plate	Thorlabs	CP02/M	Holds SM1A3TS
Mirror Holder	Thorlabs	MH25	Holds gold mirror
Mirror Mount	Thorlabs	KMSS/M	Holds MH25 on top of Piezo
Insulating cage adapter	Thorlabs	SM1A3TS	Holds microscope objective
Adapters	Machined	N/A	60mm x 60mm
Adapters	Machined	N/A	90mm x 55mm
Adapters	Machined	N/A	38mm x 25mm

Table 2. List of all the components of the FF-OCT system.

Graphical User Interface of our novel FF-OCT system

4.1 Data Acquisition and Control Signals

This chapter presents a discussion of the Graphical User Interface and the Data acquisition and switches to illustrate how our FF-OCT system acquires data acquisition and is controlled via the LabView interface. Our light source was a Supercontinuum laser, which was combined with AOTF tunable filters that were set to provide a bandwidth of ~50nm in a range of 8 wavelengths, with each having a linewidth of ~6nm with the RF driver running them. The emitted light goes directly to the FF-OCT module, and the interference pattern is detected by the camera. The system works in Time Domain and it requires the optical path distance to be matched within the coherence length of the light source. In addition, it also requires that the piezo be moved for scanning in depth. Once the system is initialized and ready (this process is explained in Section 4.2), we command the piezo to move in steps of 1 μ m, 2 μ m, or 3 μ m based on the thickness of the sample being scanned. As the piezo starts to move in steps, it signals the camera to acquire the C-scan at that moment. A C-scan is referred to as one en-face image captured by the 2D camera which is the main feature of FF-OCT. Although the camera runs at a frame rate of 100 fps, the piezo in moves in much slower steps; consequently, the camera syncs its speed with the piezo and becomes slow, acquiring a data set of 1024 images. After the raw data is acquired it is then taken to Matlab for signal processing in order to extract the information.

Figure 15 and Figure 16 show the placement of the optical module in the upper deck of the microscope and the system as a whole unit with the camera underneath, respectively.

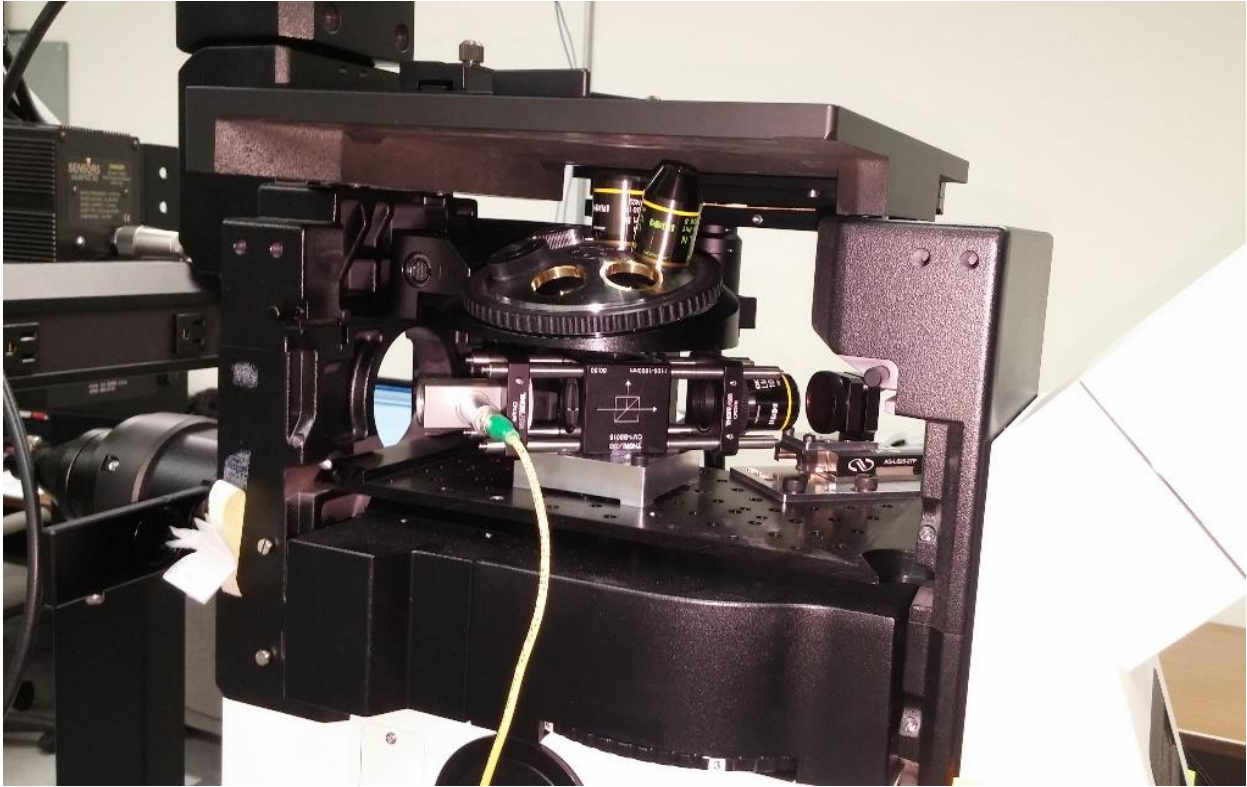


Figure 15. FF-OCT module in the second deck of our Olympus IX73 microscope.

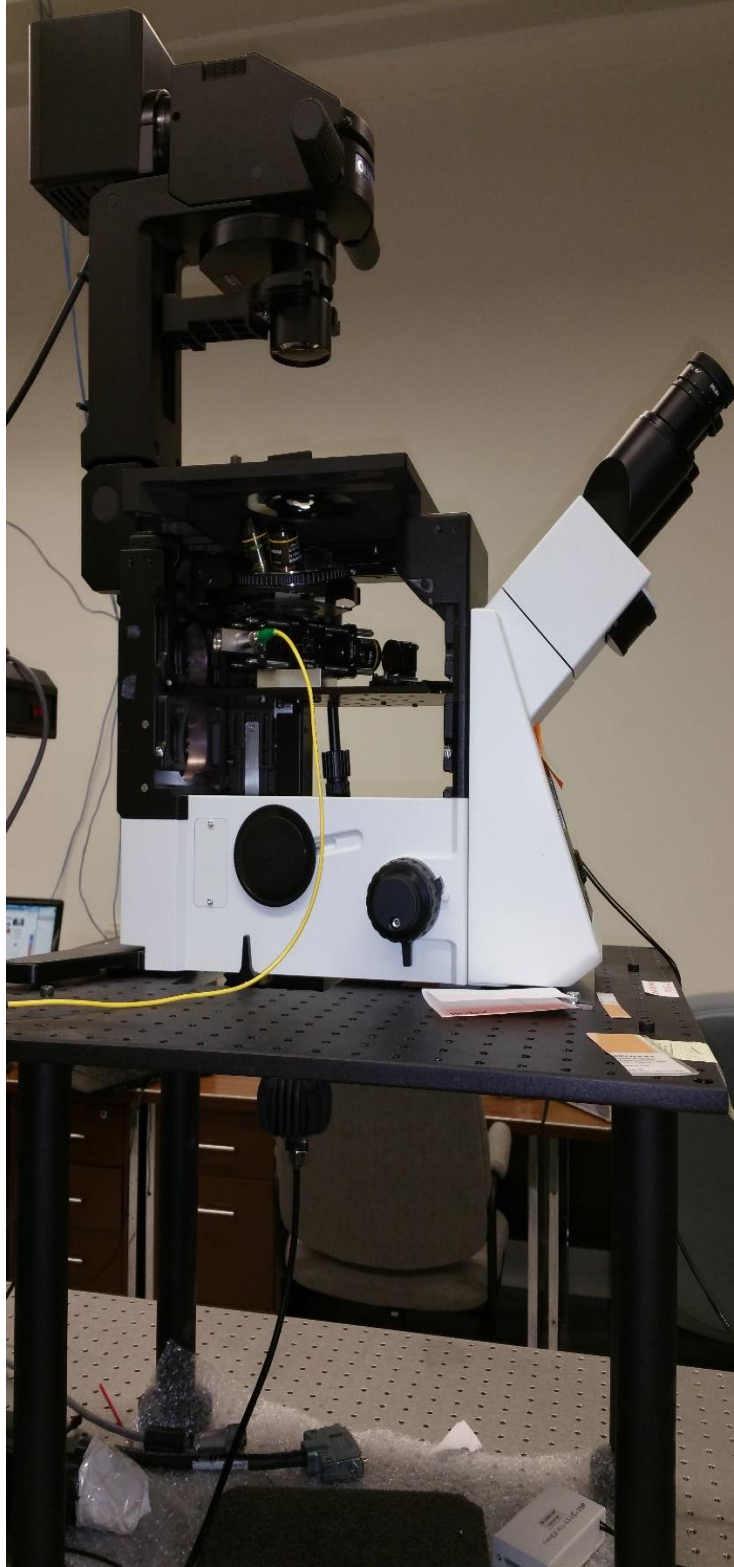


Figure 16. Olympus IX73 Microscope with FF-OCT module and Camera underneath.

4.2 Graphical User Interface (GUI)

The FF-OCT's graphical user interface was developed in LabView and is responsible for syncing all of the system's the components, including the laser and the optical module. It is a graphical language wherein coding is done in blocks called VIs, and the platform is called a block diagram. The user interface was developed on the Front Panel.

The Front Panel was oriented with ease of usability in mind. Since the system requires the prior control and configuration of several components, initialization must be done in a smooth manner. Section 4.2.1 explains the Front Panel switches, buttons, and overall actions required by the user to operate and acquire the data. In addition, Section 4.2.1 also expands on the initialization process, which was mentioned in Section 4.1. The code of LabView is given in snippet format in the Appendix 3.

4.2.1 Front Panel

As shown in Figure 17, there are three separate sections on the Front Panel (FP):

1. Camera control switches
2. Laser control switches
3. Piezoelectric-motor control switches

The function of each switch and display port(s) is explained in the sub-sections below.

4.2.1.1 Camera Control switches

Camera control switches are one of the easiest types of switches to set up and initialize because few settings are required to set up only once. However, "Snap" and "Grab" are also used quite often in data acquisition. First, we see the display screen, which shows the camera screen, light,

and interference fringes when the system is switched on. The tab marked, “Path”, is used to browse the appropriate location where the C-scans need to be saved, and the appended path shows the same location with increasing numbers of images which confirms that the data is stored. The switches “Snap” and “Grab” the function like a simple camera: “Snap” takes a still shot and then waits for the next command, and “Grab” saves images continuously unless stopped, much like a burst shot on a regular camera. Both switches take still shot(s) but in a different manner and they can be used for slower acquisitions and faster acquisitions, respectively. “Numeric” shows the number of iterations the camera has run, and “ms to wait” allows the user to slow down the camera if required. Once the LabView program has started; it automatically generates a pop-up window that is an extended controls window for the camera. This window has several functionalities and is self-explanatory in terms of its usability. In our program, this pop-up window is only used once: during initialization to set the camera’s frame rate and exposure time (shown in Figure 18). After pressing “Start”, the light on the display screen comes on and we can then work with the FP window.

4.2.1.2 Laser Control switches

The laser is initialization from the middle section where the user commands it to set multiple wavelengths and their amplitudes, as well as its current level and power level, which drive the RF driver and the AOTF. Since communication occurs on the register level of the laser’s computer chip, the user needs to press “GO” to execute each new command. Once the command is recognized, the laser will acknowledge it in the output tab or will give an error signal. All of the instructions related to the register numbers and the laser operation procedure are provided in a tabular format in the Appendix 2.

4.2.1.3 Piezo-electric motor Control switches

The right side of the program contains the Piezoelectric motor switches, which produce the delay line. The piezo's movement can be monitored and controlled via the indicators and switches in this part of the program. Under piezo electric controls section, there are three status bars. The first bar shows different commands while connecting to the piezoelectric motor, for example, "Server connection...please wait". This message does not change until the appropriate communication port for the piezo is selected. The second bar indicates the model number and other related information about the piezo. The third bar display's the piezo's status, for example, "Waiting for Piezo", "Homing" and "Ready for homing". These messages tell the user that the software is waiting for the piezo to return to its default position of 0 mm and when it is ready to move as commanded. The two other indicator bars under this piezo control section reflect the graph and movement of the piezo in waveform and numeric form to display its exact position. In addition to these indicators, there are a number of control switches. The first switch, "Step", allows the user to input any value considering 0.1 micron is the resolution of the piezo-motor, and the piezo will step forward or reverse as commanded. The switches marked "Abs. Move 1" and "Abs. Move 2" indicates the user-defined value to which the piezo continuously moves. The "# loops" switch lets the user enter any N number of steps it wants the piezo to move from the initial point in steps corresponding to the values entered in "Steps". The "Cycle" switch can be used to instruct the piezo to move in a rotation back and forth between "Abs. value 1" and "Abs. value 2". The piezoelectric motor's values can be set to a minimum and maximum value by inserting these values in the boxes marked "Set Left" and "Set Right". Finally, "Exit" stops the program completely.

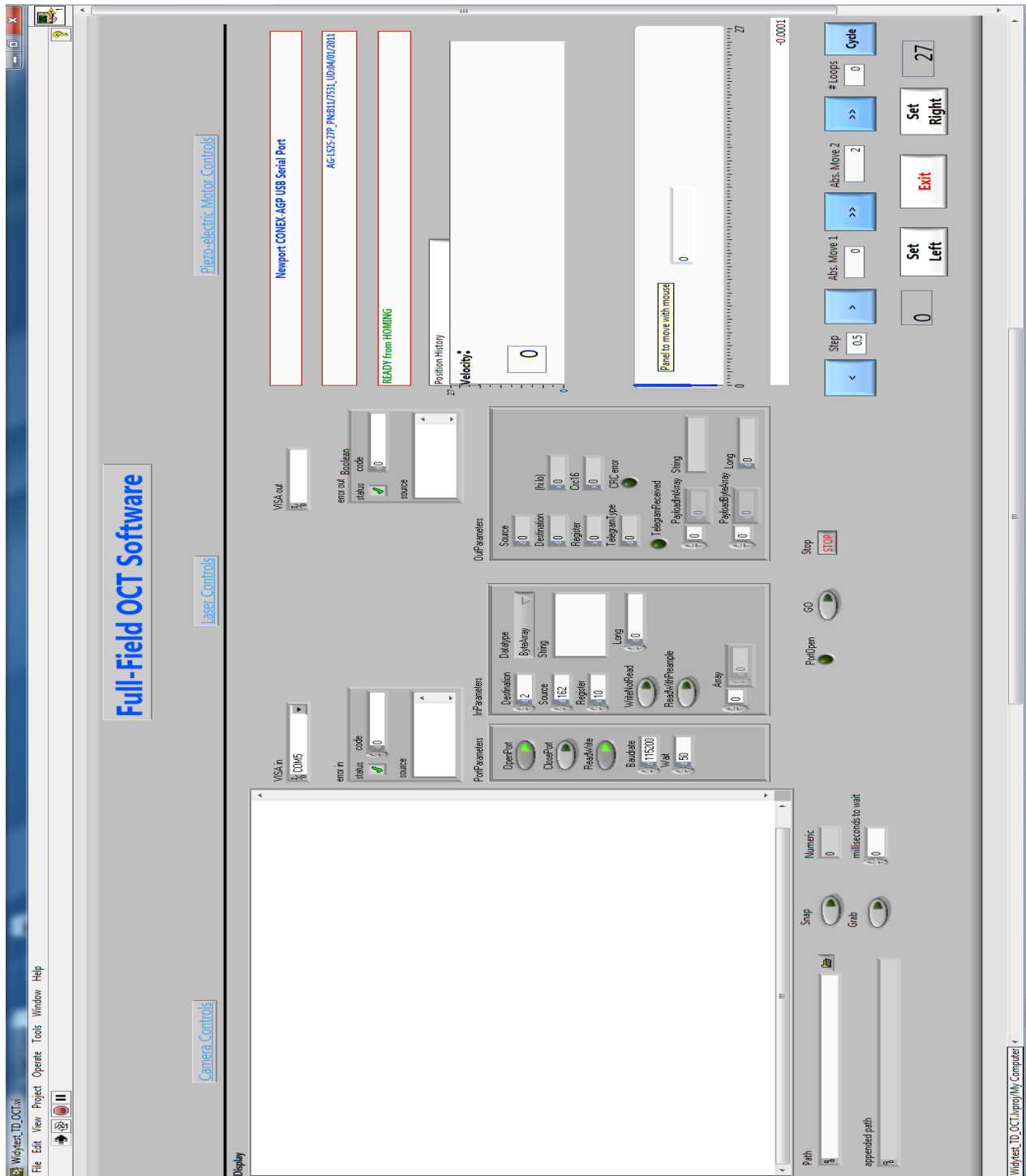


Figure 17. Front Panel of our FF-OCT GUI.

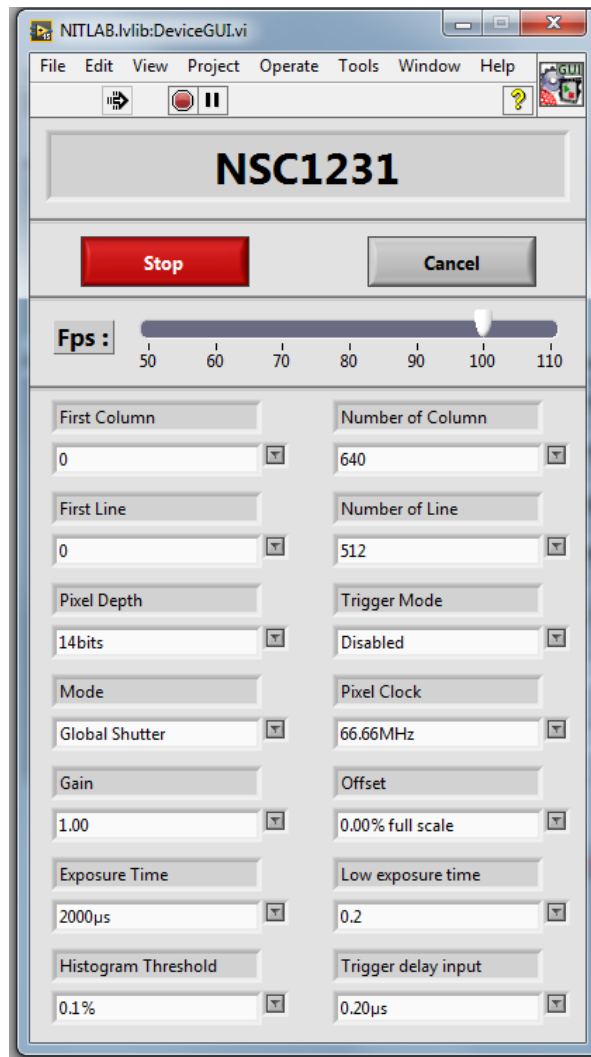


Figure 18. Extended Control panel of Camera.

Experimental Results

To verify our FF-OCT system's performance and workability, we acquired data from our sample, which was a micro cover glass slip (shown in Figure 19) with dimensions of 22mmx22mmx0.19mm. For imaging, we stacked these glass slips in sets of 3, 4, and 6 slips. We used a camera exposure time of 2000 μ s for all the three datasets, but we varied the scanning depth. For the 3 slip set, which had a total thickness of 0.57 mm (3x0.19mm), we scanned at a depth of 1mm. The other two data sets were scanned at a depth of 2mm. Although our FF-OCT system's resolution is not competitive with the general OCT system, our source's 50nm bandwidth enabled us to achieve a resolution of 15 μ m, which is reflected in the quality of the images we obtained.

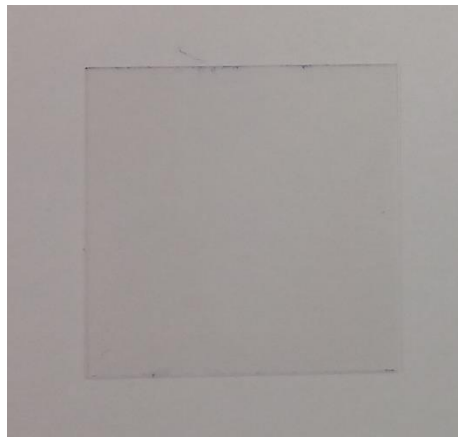


Figure 19. Micro glass coverslip (Sample).

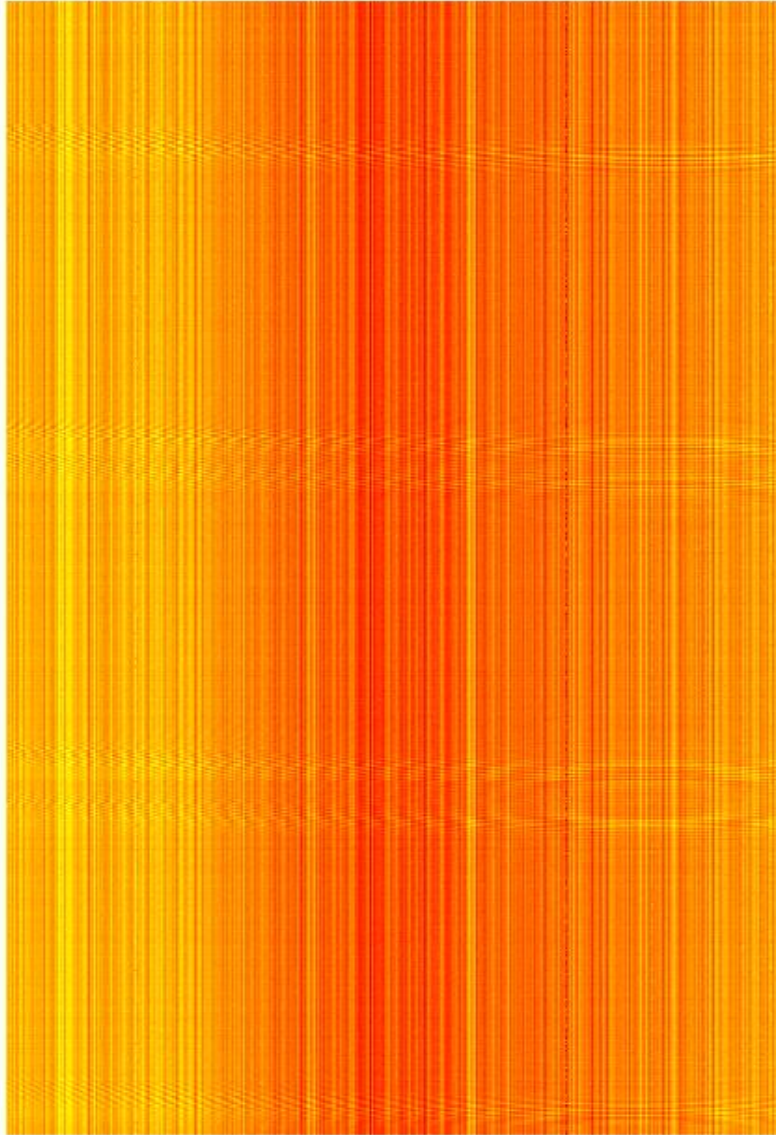


Figure 20. B-scan showing the raw data from 3 coverslips.

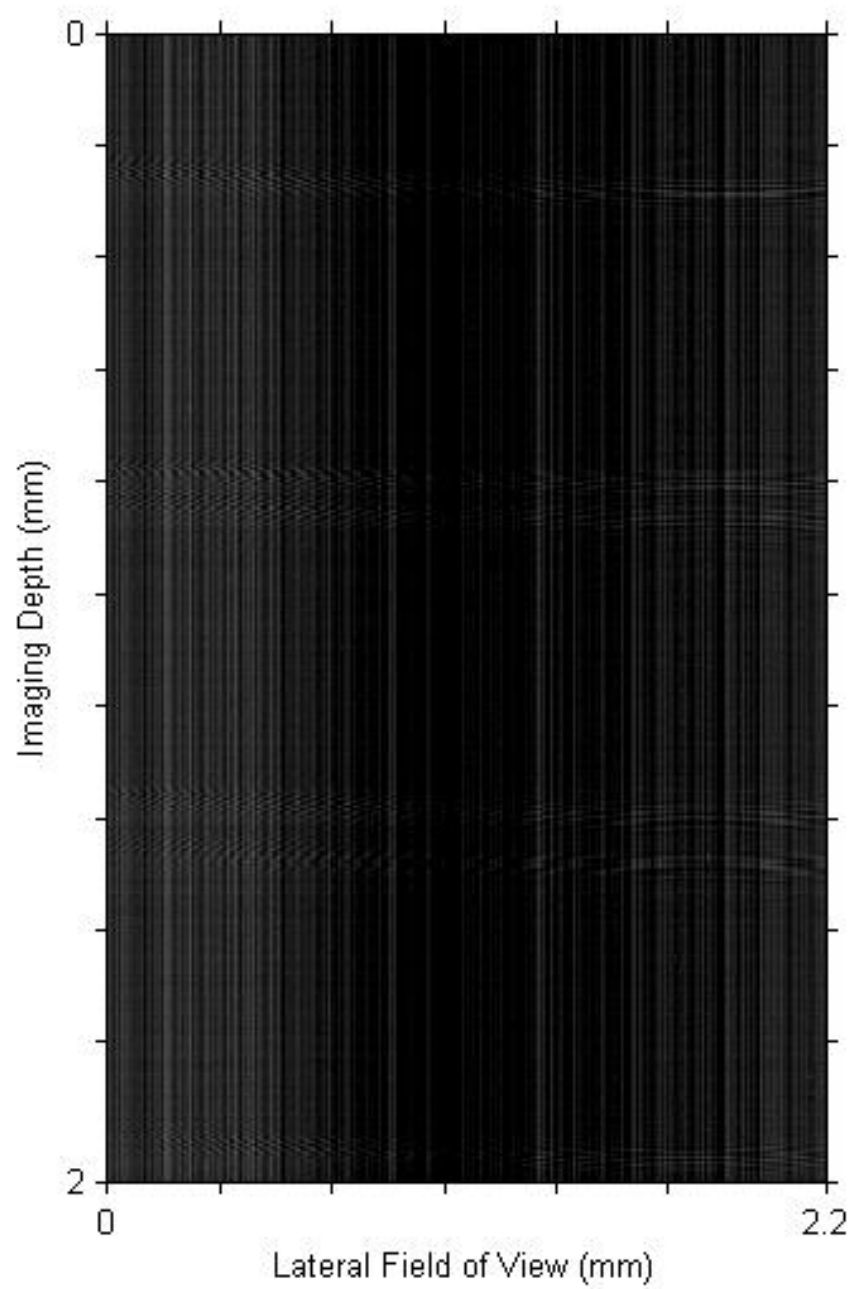


Figure 21. B-Scan showing resultant image of 3 coverslips.

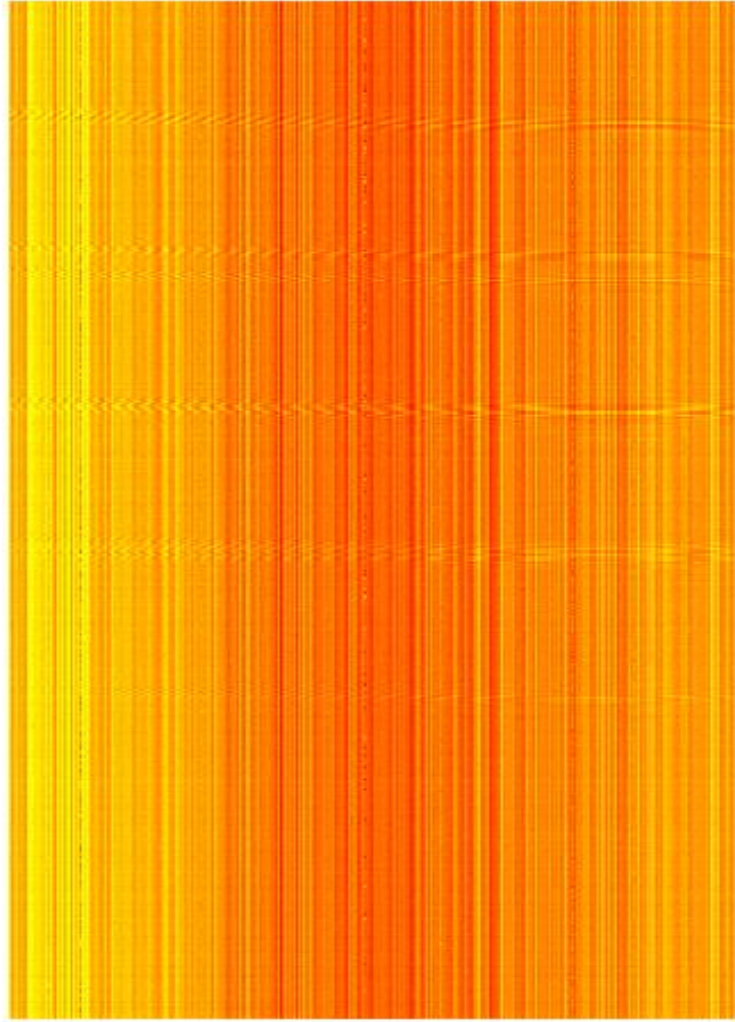


Figure 22. B-Scan showing raw data from 4 coverslips.

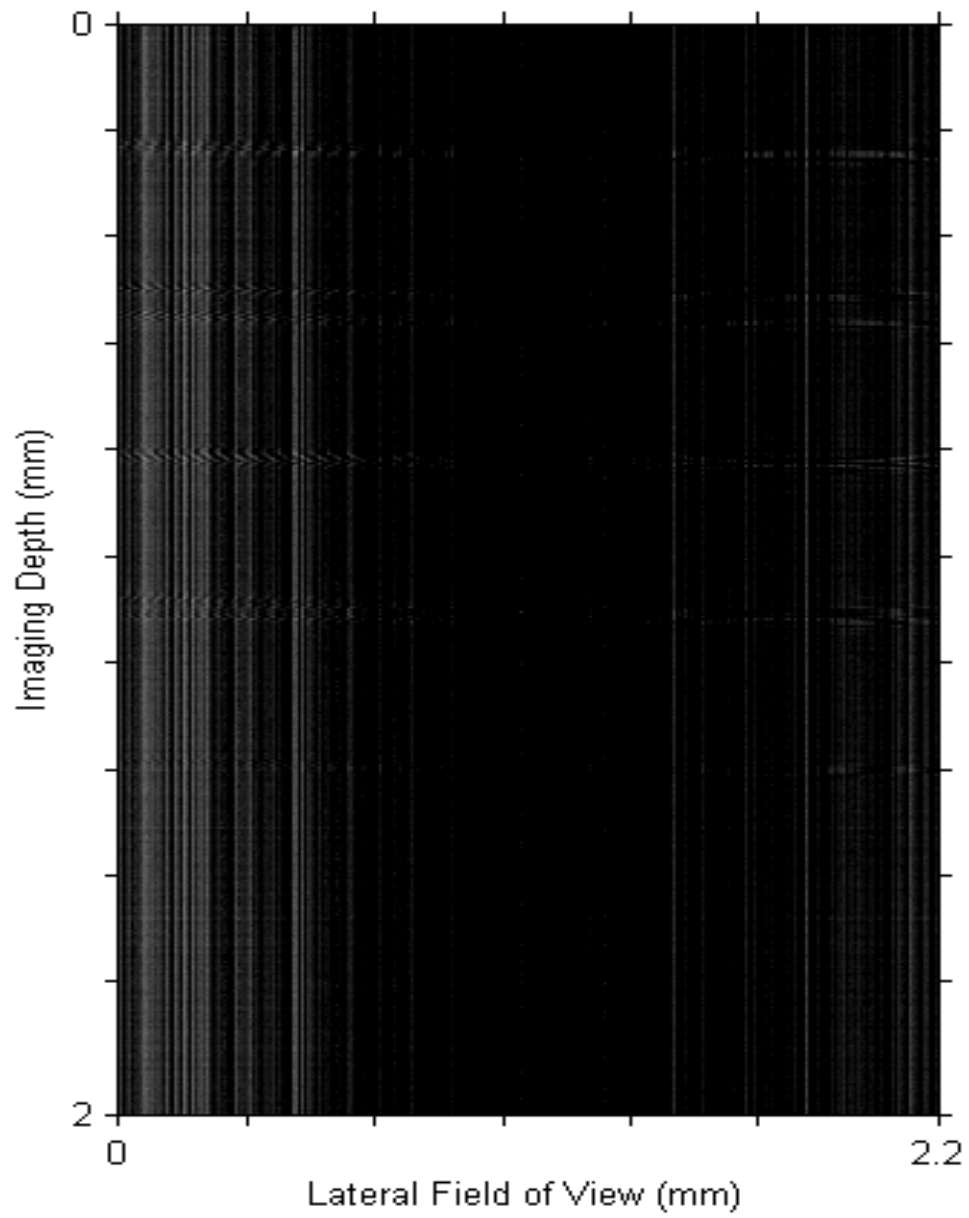


Figure 23. B-Scan showing resultant image of 4 coverslips.

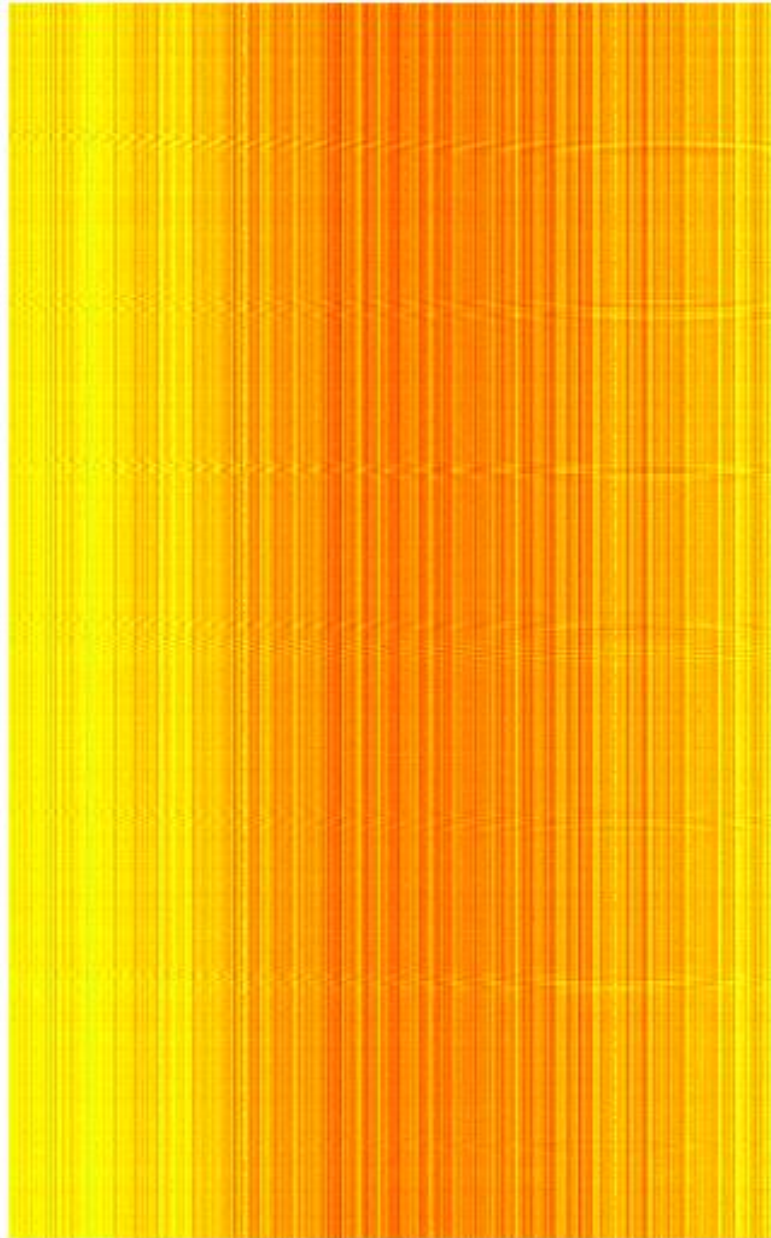


Figure 24. B-Scan showing raw data from 6 coverslips.

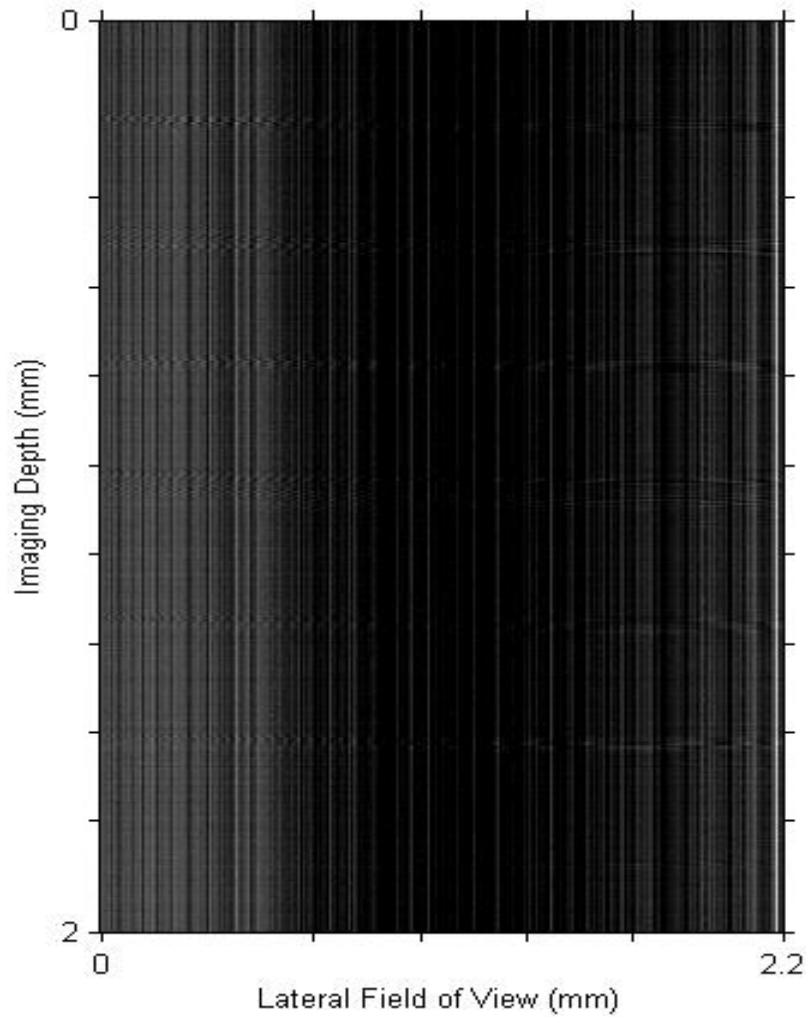


Figure 25. B-Scan showing resultant image of 6 coverslips.

In the image obtained from the 3 slip data set, we can also observe the two layers of one glass slip. In the images shown above, we can clearly see the 3, 4 and 6 slip images. To process these images, we used Hilbert Transform, which acts as a low-pass filter and which generates an analytic signal that helps to produce the signal envelope and to reproduce the images. To increase the contrast, we applied log transformation to the images; as a result, a clear difference can be seen between the raw and processed images in the results shown. We have an imaging depth of 1 μm and 2 μm respectively for stacks of 3 and 4,6 coverslips in the y-axis, having a

resolution of $\sim 20\mu\text{m}$ which is comparative to the theoretical resolution of our FF-OCT system, i.e., $\sim 17\mu\text{m}$. The noticeable vertical streaks in the images are a default product of the InGaAs camera, which does not have the Non-Uniformity Correction enabled in the LabView function. The Matlab code used for the signal processing is given in the Appendix 3.

Conclusion and Future Work

In this thesis, we have presented the design and implementation of a novel FF-OCT system on an Olympus IX73 microscope. Furthermore, we have proved that our optical module is well set up, aligned and that all the hardware components—including the laser system, the camera, and the piezo motor—function perfectly, are well synced, and can be communicated with and controlled by the LabView interface. The preliminary results of the micro glass slip tests demonstrate that we have successfully achieved our main objective: to develop and set up a FF-OCT optical module on an Olympus IX73 microscope. We believe that this is a unique project that has much future potential. To the best of our knowledge, this is the first successful attempt to develop an Optical module for OCT that can be installed on the small deck of an Olympus IX73 microscope. Moreover, this set up can be used for other types of OCT as well. Our system should be considered a hybrid system as it can be used as Time-Domain, Fourier-Domain, and Swept-Source OCT. This makes it highly unique. All of the optics and components are well-suited for use in any domain with minor changes in acquisition through LabView. There are three major possibilities for future work building on our findings:

1. Using a wideband filter to increase the bandwidth and resolution of our TD-OCT system.
2. Exploring how our FF-OCT system can be used in Fourier Domain to produce faster data acquisition.
3. Our FF-OCT system can be used to implement a SS-OCT with a traditional wavelength-swept laser by using averaging functions and frames [36][37]–[40].

Appendix 1

Phase Unwrapping in Fourier Domain based FF-OCT

An interference image at the detector consists of three sections, namely: the background image $I_0(x,y)$, the tomographic sectional image of the n^{th} layer as A_i , and the interference fringes as $\sin \phi$. The equation for this is given by [30]:

$$I(x, y) = I_0(x, y) + A_i(x, y)\sin\phi(x, y) \quad (1)$$

In order to process the data and obtain the results, the method by which the images were taken must first be determined as there are several phase unwrapping methods. These will be discussed below. The whole sample is captured in depth and volume and imaged as whole, but at different temporal and spatial positions; this is done using a phase shifting method in Fourier-Domain OCT. The phase shifts are very important and should be precisely calculated before making any movement. This is because the phase shifts are used in the calculation for the image extraction, which captures the positions of envelopes of interference images at each phase which is then transformed into a resultant image. Chang et al. and M. Akiba et al. showed different techniques used for phase unwrapping, with the former proposing an algorithm for an arbitrary phase difference value between two different interferometric images, and the latter proposing algorithm for two $\pi/2$ phase shifted images. The tomographic image recovered in both cases is given by Equations and , respectively [31] [32]

$$A_i(x, y) = ([I_1(x, y) - I_0(x, y)]^2 + \{I_2(x, y) - I_0(x, y) - [I_1(x, y) - I_0(x, y)] \cos \varphi / \sin \varphi\}^2)^{1/2} \quad (2)$$

$$A_i(x, y) = \{[I_1(x, y) - I_0(x, y)]^2 + [I_2(x, y) - I_0(x, y)]^2\}^{1/2} \quad (25)$$

However, while both of the above equations work with a known phase-shift-angle value, there are cases where the phase angles are unknown. In these cases, more data must be captured in the form of interferometric images and then solved using different 4 and 5 phase unwrapping algorithms, which are given by Equations and , respectively [30], [33], [34]:

$$A(x, y) = \left[\left(\frac{(I_1(x, y) - I_4(x, y) + I_2(x, y) - I_3(x, y))^2}{8 \sin \varphi \cos^2 \varphi} \right)^2 \right] + \left[\left(\frac{(I_1(x, y) + I_4(x, y) - I_2(x, y) - I_4(x, y))^2}{8 \sin \varphi \cos^2 \varphi} \right)^2 \right]^{0.5}, \quad (4)$$

$$\text{where } \tan \varphi = \left\{ \frac{3[I_2(x, y) - I_3(x, y)] - [I_1(x, y) - I_4(x, y)]}{I_1(x, y) - I_4(x, y) + I_2(x, y) - I_3(x, y)} \right\}^{0.5}.$$

And, for the 5 step phase-unwrapping technique:

$$A_i(x, y) = \left[\left(\frac{I_2(x, y) - I_4(x, y)}{2 \sin \varphi} \right)^2 + \left(\frac{2I_3(x, y) - I_5(x, y) - I_1(x, y)}{4 \sin^2 \varphi} \right)^2 \right]^{0.5} \quad (5)$$

$$\text{where, } \tan \varphi = \frac{2[I_2(x, y) - I_4(x, y)]}{3I_3(x, y) - I_5(x, y) - I_1(x, y)} \quad \varphi \neq n\pi.$$

Apart from these algorithms, there is one fast method that is based on the high-order derivatives of multiple sequential images that does not require phase-shift angles yet still produces multi-step phase-shifted interference images and at the detector. This method is given by [30]:

$$A_i(x, y) = \left| \left[(I_3(x, y) - 2I_2(x, y - I_1(x, y)))^2 - \{I_4(x, y) - 3[I_3(x, y) - I_2(x, y)] - I_1(x, y)\} [I_2(x, y) - I_1(x, y)] \right] \right|^{0.5} \quad (6)$$

Therefore, all the different methods discussed above refers to various algorithms for different phase steps.

Appendix 2

NKT Laser LabView Instructions and Register Values

Steps:

1. Select COM 5 in VISA IN
2. Click Open PORT, ReadWrite & press RUN. If Telegram received, then enter instructions from the table below to operate the laser.

Register Number*	Destination Number#	Instruction & Datatype	Comments
30	15(Laser)	0=Off 3=On (Long)	This will turn the emission On and Off of laser.
37	15(Laser)	The value in 0.1 (Long), E.g., 700 for 70%	This will set the laser in Const. Power level with entered value.
38	15(Laser)	The value in 0.1 (Long), E.g., 700 for 70%	This will set the laser in Const. Current level with entered value.
34	18(Select)	0= VIS/IR 1=NIR/IR	Selects Appropriate Crystal in Select.
90-97	19(RF)	The value in 0.001 (Long), E.g., 807123 for 807.123 nm	Sets appropriate Wavelength from 90- 97 register number.
B0-B7	19(RF)	The value in 0.1 (Long), E.g., 700 for 70%	Sets amplitude of appropriate wavelength from above.
30	19	0=Off 1=On	Turn on and off the RF driver and light is finally emitting from the fiber.

Table 3. Register Commands for our laser in LabView

3. To write the above commands, press the WritenotRead Command.
4. To read the values at particular addresses, keep the WritenotRead low and Run as above and this will tell you the value, the register is holding.

*Tells the appropriate register number for the function to be performed.

#Tells the destination address of where the signal/command is going.

The Table 4 below shows the meaning of Telegram Message Received from the laser after entering the register commands through LabView.

Code	Type	Description
0	NACK	Response, Message not understood, not applicable, or not allowed.
1	CRC error	Response. CRC error in received message.
2	Busy	Response. Cannot respond at the moment. Module too busy.
3	ACK	Response. Received message understood.
4	Read	Query. Read the contents of a register.
5	Write	Transmission. Write something in a register.
8	Datagram	Response. Register content returned, caused by a previous "Read".

Table 4. Telegram Message received from our Laser in Labview

Appendix 3

Matlab Code

```
clc; clear all;
i=4149;
for j=1:1:1024; %Makes a stack of data
x=imread([ num2str(i+j) '.bmp']);
z1(j ,: ,:)=x;
end
z=im2double(z1);
p=input('input the frame number\n'); %Extracts any C-scan
for k=1:1:512
for l=1:1:640;
a(k,l)=z(p,k,l);
end
end
subplot(1,3,1);
imshow(a);

m=input('frame number between 1 to 640\n');%Extracts a B-Scan from rows side
for v=1:1:j;
for w=1:1:512;
b(v,w)=z(v,w,m);
end
end
subplot(1,3,2);
imshow(b);

n=input('frame number between 1 to 512\n');%Extracts a B-Scan from Column
side
for g=1:1:j;
for h=1:1:640;
c(g,h)=z(g,n,h);
end
end
subplot(1,3,3);
imshow(c);

bh=hilbert(b);
ch=hilbert(c);

bx=b.*b;
by=bh.*bh;
bz=sqrt(bx+by);
figure;
imshow(bz);

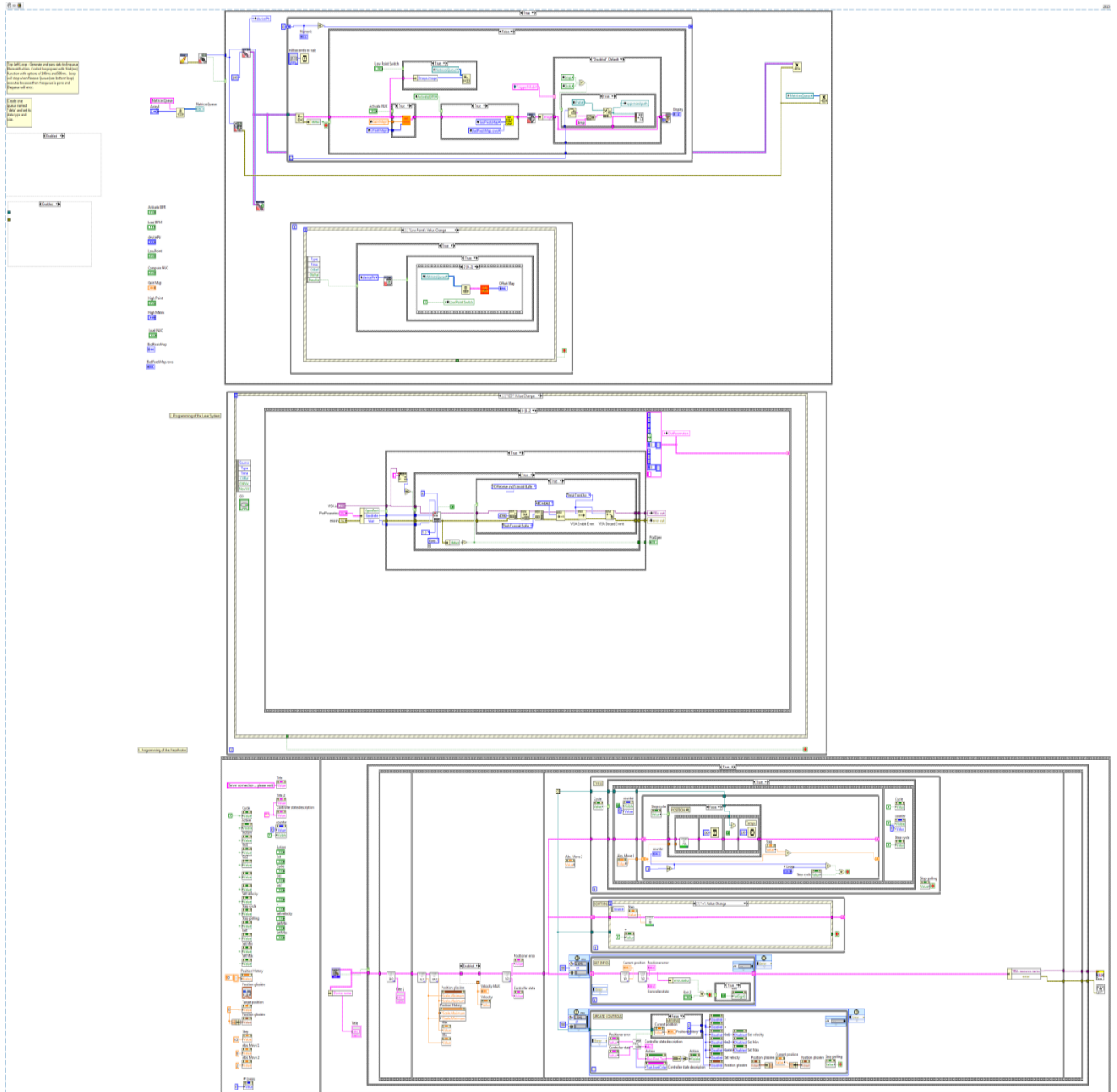
cx=c.*c;
cy=ch.*ch;
cz=sqrt(cx+cy);
figure;
imshow(cz);
m1=1.40;
lcz=m1.*log(1+cz);
```

```

figure;
imshow(lcz);
colormap('gray');
cg=gray;
cg=flipud(cg);
colormap(cg);

```

Block Diagram Of LabVIEW Code



References

- [1] D. Huang *et al.*, “Optical Coherence Tomography,” *Science*, vol. 254, no. 5035, pp. 1178–1181, Nov. 1991.
- [2] R. R. Alfano, S. G. Demos, and S. K. Gayen, “Advances in Optical Imaging of Biomedical Mediaa,” *Ann. N. Y. Acad. Sci.*, vol. 820, no. 1, pp. 248–271, May 1997.
- [3] X. Ling *et al.*, “A novel near-infrared fluorescence imaging probe that preferentially binds to cannabinoid receptors CB2R over CB1R,” *Biomaterials*, vol. 57, pp. 169–178, Jul. 2015.
- [4] C. Huang, B. Liu, and M. E. Brezinski, “Ultrasound-enhanced optical coherence tomography: improved penetration and resolution.,” *J. Opt. Soc. Am. A. Opt. Image Sci. Vis.*, vol. 25, no. 4, pp. 938–46, Apr. 2008.
- [5] P. Serranho, A. M. Morgado, and R. Bernardes, “Optical Coherence Tomography: A Concept Review,” in *Optical Coherence Tomography: A Clinical and Technical Update*, R. Bernardes and J. Cunha-Vaz, Eds. Berlin, Heidelberg: Springer Berlin Heidelberg, 2012, pp. 139–156.
- [6] R. M. P. Doornbos, R. Lang, M. C. Aalders, F. W. Cross, and H. J. C. M. Sterenberg, “The determination of in vivo human tissue optical properties and absolute chromophore concentrations using spatially resolved steady-state diffuse reflectance spectroscopy,” *Phys. Med. Biol.*, vol. 44, no. 4, pp. 967–981, Apr. 1999.
- [7] A. Kienle, L. Lilge, M. S. Patterson, R. Hibst, R. Steiner, and B. C. Wilson, “Spatially resolved absolute diffuse reflectance measurements for noninvasive determination of the

- optical scattering and absorption coefficients of biological tissue.,” *Appl. Opt.*, vol. 35, no. 13, pp. 2304–14, May 1996.
- [8] N. M. Grzywacz *et al.*, “Statistics of optical coherence tomography data from human retina.,” *IEEE Trans. Med. Imaging*, vol. 29, no. 6, pp. 1224–37, Jun. 2010.
- [9] R. Bernardes, T. Santos, P. Serranho, C. Lobo, and J. Cunha-Vaz, “Noninvasive evaluation of retinal leakage using optical coherence tomography.,” *Ophthalmol. J. Int. d’ophthalmologie. Int. J. Ophthalmol. Zeitschrift für Augenheilkd.*, vol. 226, no. 2, pp. 29–36, Jan. 2011.
- [10] V. J. Srinivasan, Y. Chen, J. S. Duker, and J. G. Fujimoto, “In vivo functional imaging of intrinsic scattering changes in the human retina with high-speed ultrahigh resolution OCT,” *Opt. Express*, vol. 17, no. 5, p. 3861, Feb. 2009.
- [11] J. Fujimoto, “Optical coherence tomography: principles and applications,” *Rev. LASER Eng. ...*, 2003.
- [12] A. Dubois, K. Grieve, G. Moneron, R. Lecaque, L. Vabre, and C. Boccara, “Ultrahigh-resolution full-field optical coherence tomography,” *Appl. Opt.*, vol. 43, no. 14, p. 2874, May 2004.
- [13] M. E. Brezinski, “Optical Coherence Tomography : Principles and Applications.”
- [14] A. (2014). Thanusutiyabhorn, Pimrapat, Sherif, Sherif, & Major, “Spectroscopic Imaging Using Quadrature Optical Coherence Tomography by Pimrapat Thanusutiyabhorn A Thesis submitted to the Faculty of Graduate Studies of The University of Manitoba in partial fulfilment of the requirements of the degree of MASTER OF SCIEN,” 2014.

- [15] M. R. Hee, B. Bouma, and G. Tearney, *Handbook of optical coherence tomography*. 2002.
- [16] C.B. Park, B.H. Joe, H.J. Hwang, E.S. Jin, and C.J. Kim, “Coronary perforation during conventional time domain optical coherence tomography.,” *Int. J. Cardiol.*, vol. 155, no. 1, pp. e14-5, Feb. 2012.
- [17] V. Gandhi, D. Semenov, S. Honkanen, and M. Hauta-Kasari, “Optical identification based on time domain optical coherence tomography.,” *Appl. Opt.*, vol. 54, no. 25, pp. 7514–9, Sep. 2015.
- [18] J. W. Cho, K. R. Sung, J. T. Hong, T. W. Um, S. Y. Kang, and M. S. Kook, “Detection of Glaucoma by Spectral Domain-scanning Laser Ophthalmoscopy/Optical Coherence Tomography (SD-SLO/OCT) and Time Domain Optical Coherence Tomography,” *J. Glaucoma*, vol. 20, no. 1, pp. 15–20, Jan. 2011.
- [19] D. Bukowska *et al.*, “Multi-parametric imaging of murine brain using spectral and time domain optical coherence tomography.,” *J. Biomed. Opt.*, vol. 17, no. 10, p. 101515, Oct. 2012.
- [20] A. F. Fercher, C. K. Hitzenberger, G. Kamp, and S. Y. El-Zaiat, “Measurement of intraocular distances by backscattering spectral interferometry,” *Opt. Commun.*, vol. 117, no. 1–2, pp. 43–48, May 1995.
- [21] M. Wojtkowski, R. Leitgeb, A. Kowalczyk, T. Bajraszewski, and A. F. Fercher, “In vivo human retinal imaging by Fourier domain optical coherence tomography.,” *J. Biomed. Opt.*, vol. 7, no. 3, pp. 457–63, Jul. 2002.
- [22] Z. Yaqoob, J. Wu, and C. Yang, “Spectral domain optical coherence tomography: a better

- OCT imaging strategy,” *Biotechniques*, 2005.
- [23] A. Dubois, J. Moreau, and C. Boccara, “Spectroscopic ultrahigh-resolution full-field optical coherence microscopy,” *Opt. Express*, vol. 16, no. 21, pp. 17082–520533, 2008.
- [24] T. Bonin, G. Franke, M. Hagen-Eggert, P. Koch, and G. Hüttmann, “In vivo Fourier-domain full-field OCT of the human retina with 1.5 million A-lines/s.,” *Opt. Lett.*, vol. 35, no. 20, pp. 3432–3434, 2010.
- [25] A. Dubois, “Full-Field Optical Coherence Microscopy.”
- [26] J. Ogien and A. Dubois, “High-resolution full-field optical coherence microscopy using a broadband light-emitting diode,” *Opt. Express*, vol. 24, no. 9, p. 9922, May 2016.
- [27] A. Federici and A. Dubois, “Full-field optical coherence microscopy with optimized ultrahigh spatial resolution,” *Opt. Lett.*, vol. 40, no. 22, p. 5347, Nov. 2015.
- [28] W. Y. Oh, B. E. Bouma, N. Iftimia, S. H. Yun, R. Yelin, and G. J. Tearney, “Ultrahigh-resolution full-field optical coherence microscopy using InGaAs camera,” *Opt. Express*, vol. 14, no. 2, p. 726, Jan. 2006.
- [29] A. Dubois, L. Vabre, A.-C. Boccara, and E. Beaurepaire, “High-resolution full-field optical coherence tomography with a Linnik microscope,” *Appl. Opt.*, vol. 41, no. 4, p. 805, Feb. 2002.
- [30] S. Chang, X. Cai, and C. Flueraru, “An efficient algorithm used for full-field optical coherence tomography,” *Opt. Lasers Eng.*, vol. 45, no. 12, pp. 1170–1176, 2007.
- [31] S. Chang, X. Liu, X. Cai, and C. P. Grover, “Full-field optical coherence tomography and its application to multiple-layer 2D information retrieving,” *Opt. Commun.*, vol. 246, no.

- 4, pp. 579–585, 2005.
- [32] M. Akiba, K. P. Chan, and N. Tanno, “Full-field optical coherence tomography by two-dimensional heterodyne detection with a pair of CCD cameras,” *Opt. Lett.*, vol. 28, no. 10, p. 816, May 2003.
- [33] J. H. B. J.E. Greivenkamp, *Optical shop testing. Phase shift interferometer*, Second. Wiley, 1992.
- [34] P. Hariharan, B. F. Oreb, and T. Eiju, “Digital phase-shifting interferometry: a simple error-compensating phase calculation algorithm,” *Appl. Opt.*, vol. 26, no. 13, p. 2504, Jul. 1987.
- [35] E. Cuche, P. Marquet, P. Dahlgrenz, and C. Depeursinge, “Digital Holographic Microscopy, a new Method for Simultaneous Amplitude-and Quantitative Phase-Contrast Imaging.”
- [36] K. Gr and M. S. Classification, “Reconstruction of signals from Irregular sampling,,” vol. 59, no. 199, pp. 181–194, 1992.
- [37] W. Sun and X. Zhou, “Reconstruction of band-limited signals from local averages,” *IEEE Trans. Inf. Theory*, vol. 48, no. 11, pp. 2955–2963, 2002.
- [38] H. Schwab, “Reconstruction from averages,” 2003.
- [39] J. Kovačević and A. Chebira, “An Introduction to Frames,” *Found. Trends® Signal Process.*, vol. 2, no. 1, pp. 1–94, 2007.
- [40] J. J. Benedetto and P. J. S. G. Ferreira, *Modern Sampling Theory: Mathematics and Applications*. Birkhäuser Boston, 2001.